The Astrophysical Journal, 837:161 (22pp), 2017 March 10 https://doi.org/10.3847/1538-4357/aa62a7

Comparing Submillimeter Polarized Emission with Near-infrared Polarization of Background Stars for the Vela C Molecular Cloud

Fabio P. Santos[1], Peter A. R. Ade[2], Francesco E. Angilè[3], Peter Ashton[1], Steven J. Benton[4,5], Mark J. Devlin[3], Bradley Dober[3], Laura M. Fissel[1], Yasuo Fukui[6], Nicholas Galitzki[3], Natalie N. Gandilo[7,8], Jeffrey Klein[3], Andrei L. Korotkov[9], Zhi-Yun Li[10], Peter G. Martin[11], Tristan G. Matthews[1], Lorenzo Moncelsi[12], Fumitaka Nakamura[13], Calvin B. Netterfield[4,7], Giles Novak[1], Enzo Pascale[2], Frédérick Poidevin[14,15], Giorgio Savini[16], Douglas Scott[17], Jamil A. Shariff[7,18], Juan Diego Soler[19], Nicholas E. Thomas[20], Carole E. Tucker[2], Gregory S. Tucker[9], and Derek Ward-Thompson[21]

[1] Center for Interdisciplinary Exploration and Research in Astrophysics (CIERA) and Department of Physics & Astronomy, Northwestern University, 2145 Sheridan Road, Evanston, IL 60208, USA
[2] Cardiff University, School of Physics & Astronomy, Queens Buildings, The Parade, Cardiff CF24 3AA, UK
[3] Department of Physics & Astronomy, University of Pennsylvania, 209 South 33rd Street, Philadelphia, PA 19104, USA
[4] Department of Physics, University of Toronto, 60 St. George Street Toronto, ON M5S 1A7, Canada
[5] Department of Physics, Princeton University, Jadwin Hall, Princeton, NJ 08544, USA
[6] Department of Physics and Astrophysics, Nagoya University, Nagoya 464-8602, Japan
[7] Department of Astronomy & Astrophysics, University of Toronto, 50 St. George Street, Toronto, ON M5S 3H4, Canada
[8] Department of Physics and Astronomy, Johns Hopkins University, 3701 San Martin Drive, Baltimore, MD, USA
[9] Department of Physics, Brown University, 182 Hope Street, Providence, RI 02912, USA
[10] Department of Astronomy, University of Virginia, 530 McCormick Road, Charlottesville, VA 22904, USA
[11] CITA, University of Toronto, 60 St. George St., Toronto, ON M5S 3H8, Canada
[12] California Institute of Technology, 1200 E. California Boulevard, Pasadena, CA 91125, USA
[13] National Astronomical Observatory, Mitaka, Tokyo 181-8588, Japan
[14] Instituto de Astrofisica de Canarias, E-38200 La Laguna, Tenerife, Spain
[15] Universidad de La Laguna, Dept. Astrofísica, E-38206 La Laguna, Tenerife, Spain
[16] Department of Physics & Astronomy, University College London, Gower Street, London, WC1E 6BT, UK
[17] Department of Physics & Astronomy, University of British Columbia, 6224 Agricultural Road, Vancouver, BC V6T 1Z1, Canada
[18] Department of Physics, Case Western Reserve University, 2076 Adelbert Road, Cleveland, OH, 44106-7079, USA
[19] Institute d'Astrophysique Spatiale, CNRS (UMR8617) Université Paris-Sud 11, Bâtiment 121, Orsay, France
[20] NASA/Goddard Space Flight Center, Greenbelt, MD 20771, USA
[21] Jeremiah Horrocks Institute, University of Central Lancashire PR1 2HE, UK
Received 2016 May 27; revised 2017 February 6; accepted 2017 February 21; published 2017 March 15

Abstract

We present a large-scale combination of near-infrared (near-IR) interstellar polarization data from background starlight with polarized emission data at submillimeter wavelengths for the Vela C molecular cloud. The near-IR data consist of more than 6700 detections probing a range of visual extinctions between 2 and 20 mag in and around the cloud. The submillimeter data were collected in Antarctica by the Balloon-borne Large Aperture Submillimeter Telescope for Polarimetry. This is the first direct combination of near-IR and submillimeter polarization data for a molecular cloud aimed at measuring the "polarization efficiency ratio" ($R_{\rm eff}$), a quantity that is expected to depend only on grain-intrinsic physical properties. It is defined as $p_{500}/(p_I/\tau_V)$, where p_{500} and p_I are polarization fractions at 500 μm and the I band, respectively, and τ_V is the optical depth. To ensure that the same column density of material is producing both polarization from emission and from extinction, we conducted a careful selection of near-background stars using 2MASS, *Herschel*, and *Planck* data. This selection excludes objects contaminated by the Galactic diffuse background material as well as objects located in the foreground. Accounting for statistical and systematic uncertainties, we estimate an average $R_{\rm eff}$ value of 2.4 ± 0.8, which can be used to test the predictions of dust grain models designed for molecular clouds when such predictions become available. The ratio $R_{\rm eff}$ appears to be relatively flat as a function of the cloud depth for the range of visual extinctions probed.

Key words: dust, extinction – ISM: magnetic fields – ISM: individual objects (Vela C molecular cloud) – techniques: polarimetric

1. Introduction

Astronomers have known about the existence of magnetic fields in the interstellar medium (ISM) for over 60 years, as initially revealed by observations of starlight polarization (Hall 1949; Hiltner 1949; Davis & Greenstein 1951; Mathewson & Ford 1970; Serkowski et al. 1975). From the diffuse neutral material to molecular clouds and dense cores, polarimetry of starlight and polarized thermal emission from dust have historically proved to be the best tracers of the sky-projected component of the magnetic field. Despite extensive efforts to understand the role of magnetic fields in the ISM, many open questions remain. For example, although molecular clouds are widely known to be sites of star formation, the role of magnetic fields in this process is not entirely understood. Molecular clouds exhibit intricate patterns of filaments and striations, but the relation of these structures to magnetic fields is still under debate (Goldsmith et al. 2008; André et al. 2010; Arzoumanian et al. 2011). Furthermore, we do not know whether magnetic fields are able to support clouds against gravitational collapse, thereby affecting the efficiency for forming new stars (Mouschovias & Paleologou 1981; McKee & Ostriker 2007).

Although the above-mentioned magnetic field mapping technique is now widely used, the detailed mechanisms regulating

polarized emission and extinction by dust are not entirely understood. Starlight of background objects becomes linearly polarized after passing through an interstellar cloud in which a subset population of nonspherical grains have their long axis preferentially aligned perpendicular to the magnetic field (Hall 1949; Hiltner 1949; Davis & Greenstein 1951; Mathewson & Ford 1970). The observed polarization orientation will be parallel to the sky-projected magnetic field. The degree of polarization of background starlight is detectable in the ultraviolet, peaks in the optical ($\lambda \approx 0.55\ \mu$m), and falls off in the near-infrared (near-IR) spectral bands (Serkowski et al. 1975). This wavelength dependence gives clues regarding the size distribution of aligned particles (Kim & Martin 1994, 1995). Aligned dust grains radiate thermally at wavelengths longer than the mid-infrared spectral bands (according to their typical temperatures of ~10–100 K), and this emission is polarized perpendicularly to the magnetic field (Hildebrand 1983, 1988).

The limitations in interpreting polarization data from extinction or emission are usually related to uncertainties regarding the alignment mechanism or the physical properties of the dust grains. The most promising grain alignment theory, known as radiative torques (RATs; Dolginov & Mitrofanov 1976; Draine & Weingartner 1996, 1997; Lazarian & Draine 2000; Lazarian 2007), requires an anisotropic radiation field having $\lambda \sim a$, where a is the grain size. This is consistent with evidence that inside starless cores there is a depth beyond which no alignment takes place (Whittet et al. 2008; Alves et al. 2014; Jones et al. 2015). Other observations consistent with the predictions of RATs include the poor alignment of small-sized grains (Kim & Martin 1995) and the angular dependence of polarization efficiency around sources of radiation, relative to the magnetic field direction (Andersson et al. 2011; Vaillancourt & Andersson 2015). However, the classical alignment mechanism (paramagnetic relaxation; Davis & Greenstein 1951) may still be significant for a subset of smaller-sized grains (Hoang et al. 2014), suggesting a balance between both effects (for a review see Andersson et al. 2015).

The most basic observational constraint on dust properties that can be derived from interstellar polarimetry is that a fraction of the grain population must be nonspherical, a necessary condition to produce polarization. The grain composition is primarily silicates and carbonaceous material (for a review see Draine 2003). Spectropolarimetry of silicate spectral features shows that silicate grains are subject to alignment mechanisms (Smith et al. 2000). By contrast, the nondetection of polarization levels in spectral features associated with carbonaceous grains suggests that these are generally not aligned (Chiar et al. 2006), but more study is needed. In general, it is possible to draw conclusions regarding grain properties by comparing observations of the polarization spectra to predictions based on physical grain models (e.g., Bethell et al. 2007; Draine & Fraisse 2009). The predictions can be adjusted by varying a range of input parameters.

The fractional polarization levels detected in extinction and emission ($p_{\rm ex}$ and $p_{\rm em}$, respectively) are strongly affected by the grain alignment conditions (i.e., the alignment efficiency), grain intrinsic properties (shapes, sizes, and chemical compositions), and the inclination of magnetic fields to the line of sight (LOS). For polarization by extinction, the polarization degree generally increases linearly with the amount of material distributed along the LOS (Jones 1989), so normalizing this quantity by the visual optical depth ($p_{\rm ex}/\tau_V$) makes it a suitable probe of the polarization efficiency, analogous to $p_{\rm em}$. In view of all the variables that can affect $p_{\rm em}$ and $p_{\rm ex}/\tau_V$, it is useful to find quantities that are invariant with respect to one or another of these physical parameters, allowing their combined effect to be disentangled. One of these quantities is the "polarization efficiency ratio," defined as $p_{\rm em}/(p_{\rm ex}/\tau_V)$. Assuming a situation in which the same population of dust grains distributed along the LOS produces both polarization by emission and by extinction, $p_{\rm em}$ and $p_{\rm ex}/\tau_V$ are expected to be equally dependent on alignment efficiencies and inclinations of magnetic fields to the LOS. Therefore, their ratio should depend only on properties inherent to the grains themselves, such as emission and extinction cross sections, which in turn depend on their shapes and dielectric functions (Hildebrand 1988; Martin 2007; Jones et al. 2015; Jones 2015). Therefore the polarization efficiency ratio is a powerful probe of dust properties over a wide range of densities and temperatures, and it is particularly interesting to compare against grain models that relate $p_{\rm em}$ to $p_{\rm ex}/\tau_V$ using a range of adjustable parameters (Draine & Fraisse 2009).

The main goal of the work presented here is to determine $p_{\rm em}/(p_{\rm ex}/\tau_V)$ for the Vela C molecular cloud, which is a portion of a larger complex of clouds known as the Vela Molecular Ridge (VMR; Murphy & May 1991; Netterfield et al. 2009). Vela C is located at a distance of 700 ± 200 pc (Liseau et al. 1992). This cloud was the main observational target of BLASTPol (the Balloon-borne Large Aperture Submillimeter Telescope for Polarimetry), which conducted deep submillimeter observations of the polarized thermal emission from the cloud (Fissel et al. 2016). We report the results of an extensive observational survey of near-IR stellar polarization for a wide portion of the cloud, providing over 6700 detections. This enabled us to carry out a large-scale combination of polarization from extinction and emission, in which complementary data from 2MASS, *Herschel,* and *Planck* were also utilized. Section 2 describes the observations and data reduction scheme for both the submillimeter and near-IR samples. In Section 3 we compare the magnetic field angles inferred respectively from submillimeter and near-IR data. In Section 4 we introduce a major challenge in the analysis, which is our lack of prior knowledge concerning stellar distances. We show how the above-mentioned complementary data can give us a handle on this problem. Section 5 describes the computation of the polarization efficiency ratio $p_{\rm em}/(p_{\rm ex}/\tau_V)$, for which we adopt the symbol $R_{\rm eff}$. A discussion of the results is given in Section 6, and our main conclusions are summarized in Section 7.

2. Observational Data

2.1. Polarized Thermal Emission from BLASTPol

BLASTPol is a high-altitude balloon-borne experiment that was launched on 2012 December 26 from Antarctica. It was equipped with a 1.8 m diameter primary mirror and a series of dichroic filters that allowed us to carry out simultaneous observations of total intensity I in three spectral bands centered at 250, 350, and 500 μm. Additionally, using a polarizing grid mounted in front of the detector arrays, together with an achromatic half-wave plate (HWP; Moncelsi et al. 2014), BLASTPol was able to measure the linear polarization Stokes parameters Q and U. A thorough description of the instrument and the observational strategy adopted, as well as the data

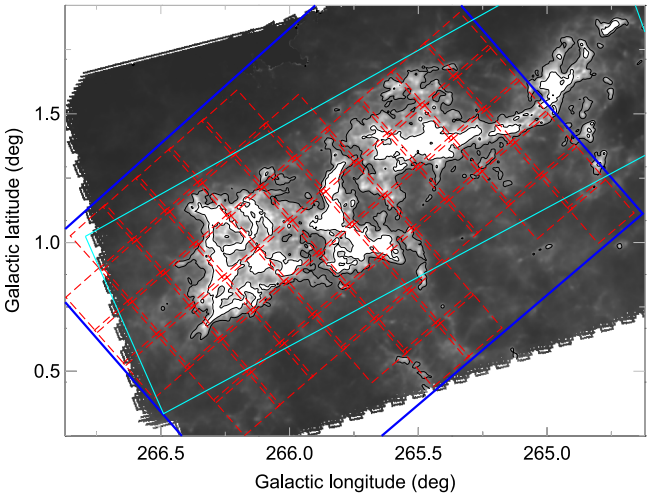

Figure 1. Column density image of Vela C (obtained from *Herschel* data, as described in Section 4.3), with contours representing the cloud's visual extinction ($A_V^{\rm cl}$) at levels of 10 and 25 mag. The red dashed-line mosaic shows observation fields used in the *I*-band survey, and the cyan box represents the "validity region" for the BLASTPol data set (see Section 2.3). The blue box is the area used to retrieve near-IR photometric data from 2MASS (Section 4.2). Stellar objects located both in this box and within the boundaries of the *Herschel* map define the "wide photometric field" (see Table 1).

reduction, beam analysis, and null tests for data quality assurance, may be found in Fissel et al. (2016).

Although BLASTPol targeted various Galactic molecular clouds, Vela C was its highest-priority science target. We carried out a "deep" 43 hr integration toward the densest portions of the cloud (more specifically, covering four of the five Vela C subregions defined by Hill et al. 2011). In addition, an extra 11 hr of integration were spent on a wider area around the cloud ($\sim$10 deg^2), consisting of more diffuse interstellar material. The observing mode involved a series of raster scans, using four different HWP angles.

For the purposes of this work, we are focusing only on the 500 μm data set. Polarimetry at 250 and 350 μm and its relationship with polarimetry at 500 μm are discussed in a separate work (Gandilo et al. 2016). As described by Fissel et al. (2016), for this particular set of observations, our beam FWHM was larger than had been predicted by our optics model, containing significant structure with a non-Gaussian shape. The data were smoothed in order to obtain an approximately round beam having an FWHM of 2.′5.

2.2. Near-IR Polarization from OPD

The near-IR polarization data were acquired at the Pico dos Dias Observatory (OPD[22], Brazil) in a series of observations between 2013 November and 2014 February. Both the 1.6 m and the 0.6 m telescopes were used in alternating night shifts, together with the IAGPOL polarimeter with the *I*-band near-IR filter (0.79 μm, Cousins) and the optical CCD detector. In both telescopes, the detector covers a field of view of approximately $11' \times 11'$, and therefore a careful mosaic-mapping was needed in order to cover a large portion of the molecular cloud. In Figure 1, the red dashed boxes represent each of the 62 areas observed in the *I* band.

The polarimeter (Magalhaes et al. 1996) consists of a sequence of optical elements positioned in the optical path. The incident light first passes through an achromatic HWP (with an optical axis orientation of ψ), which is made to rotate in discrete steps of 22.°5. Next, a Savart analyzer splits the beam into two orthogonally polarized components. These components then pass through a spectral filter, and the duplicated stellar images are simultaneously detected by the CCD. Sequential rotations of the HWP cause flux variations in the orthogonally polarized components, so the flux ratios can be fit to a modulation function proportional to $\bar{Q}\cos 4\psi + \bar{U}\sin 4\psi$ ($\bar{Q} = Q/I$ and $\bar{U} = U/I$ are the flux-normalized Stokes parameters, where I is the total intensity). Since the polarimetric quantities are derived from flux ratios, the observational strategy is essentially analogous to differential photometry, and any atmospheric variations are canceled through this operation.

For all 62 observational fields, two independent sets of observations were carried out respectively using short (10–20 s) and long (60–100 s) exposure times, at each of the eight positions of the HWP. In cases where a single object was observed multiple times, the measurement with the highest signal-to-noise ratio (S/N) was selected. At least three polarimetric standard stars were observed each night (Hsu & Breger 1982; Clemens & Tapia 1990; Turnshek et al. 1990; Larson et al. 1996), in order to calibrate the polarization position angles and check the consistency of the instrumental polarization (which can be safely neglected for this instrumental set, considering that it is much smaller than the typical uncertainties of $\approx$0.1%).

The data reduction process consisted of standard image treatment (bias, flat-fielding, and bad-pixel correction), followed by aperture photometry of all duplicated images of point-like sources. The resulting fluxes were subsequently used to build modulation functions for each object using a set of specifically designed IRAF[23] routines (PCCDPACK, Pereyra 2000). The polarization degree p_I and orientation θ_I as well as their respective uncertainties were calculated for each object based on the corresponding normalized Stokes parameters. A detailed description of the data processing can be found in Santos et al. (2012).

2.3. Corrections Applied to BLASTPol and I-band Polarization Data

Before carrying out a comparison between near-IR and submillimeter polarimetric data, a set of data corrections and selections must be carried out in order to make sure that only a high-quality subsample is used for the comparison. Table 1 summarizes the corrections and selections for the various data sets that are used in this work. The corrections are described in the present subsection.

To define both the basic BLASTPol and the basic *I*-band data sets, we first apply the debiasing correction according to the prescription $p \rightarrow \sqrt{p^2 - \sigma_p^2}$ (Wardle & Kronberg 1974), which is not valid for lower S/N data (the low S/N data will

[22] The Pico dos Dias Observatory is operated by the Brazilian National Laboratory for Astrophysics (LNA), a research institute of the Ministry of Science, Technology and Innovation (MCTI).

[23] IRAF is distributed by the National Optical Astronomy Observatories, which are operated by the Association of Universities for Research in Astronomy, Inc., under cooperative agreement with the National Science Foundation (Tody 1986).

Table 1
Selection Criteria for the Data Sets Used in the Analysis

Data Set Denomination	Source	Selection ID	Selection Criteria	N	Figures
Basic BLASTPol	BLASTPol	S1	Debiasing ($p_{500} \rightarrow \sqrt{p_{500}^2 - \sigma_{p500}^2}$), consistency between aggressive and conservative diffuse background subtraction methods (see Section 2.4), data inside the validity region (cyan, Figure 1) $p_{500}/\sigma_{p500} > 3$	3157[a]	2 (red pseudovectors)
Basic *I*–band	OPD	S2	Debiasing ($p_I \rightarrow \sqrt{p_I^2 - \sigma_{pI}^2}$), $p_I/\sigma_{pI} > 3$	6740	2 (cyan pseudovectors)
Basic polarization combination	BLASTPol, OPD	S3	Selections S1 and S2, areas of overlap between submillimeter and *I*-band pseudovectors	1355[a]	3
Wide photometric field	2MASS, Herschel	S4	Stars inside blue box (Figure 1) and within the boundaries of the *Herschel* map, 2MASS "AAA" quality, points inside reddening band (blue, Figure 5)	20348	5, 6, 8 (black dots), 15
Planck–2MASS combination	*Planck*, 2MASS, *Herschel*	S5	Same objects from the wide photometric field (selected using S4) combined to *Planck* τ_{353} data	20348	7
I-band–2MASS combination	OPD, 2MASS	S6	Selection S2, 2MASS "AAA" quality, points inside reddening band (blue, Figure 5)	5980	14
Corrected polarization combination	BLASTPol, OPD, 2MASS, *Herschel*	S7	Selections S3 and S4, magnetic field orientation consistency ($\Delta\theta < 15°$) and removal of RCW 36 area (see Section 3.2), foreground correction (see Section 5.1) with $p_I/\sigma_{pI} > 3$ reapplied, $A_V^{st}/\sigma A_V^{st} > 3$	834[a]	8 (red crosses), 11
Ideal stellar sample	BLASTPol, OPD, 2MASS, *Herschel*	S8	Selections S7, points within the ideal stellar locus (see Figure 8)	87[a,b]	9, 10

Notes. The table shows a list of selection criteria for each data set used in this work. The columns respectively represent the adopted denomination of the data set, the source of the data set itself, and the data products used to apply the selection, an identifier (ID) to specify the list of selections, the selection criteria applied to each data set, the number of data points (N) obtained after selection, and the figures where each data set is used for analysis.

[a] Valid for the intermediate diffuse emission subtraction method.

[b] Average number considering systematic variations of the GL method (see Appendix D).

later be rejected, as discussed in Section 2.4). Second, it is necessary to remove from the BLASTPol data set the contribution from the diffuse Galactic emission (foreground and background), thereby isolating only the polarized dust emission from the Vela C molecular cloud itself. This process is described in detail by Fissel et al. (2016). It was carried out using two different methods. In the first method, which we refer to as "conservative," we assume that most of the diffuse emission near Vela C is actually associated with the cloud, and therefore the goal was to avoid subtracting such emission. This was achieved by using a well-separated nearby low-flux region (also mapped by BLASTPol) as a representation for the background/foreground dust emission. In this subtraction method, we are effectively assuming that the background/foreground emission is uniform across the region. In the second method, referred to as "aggressive," the diffuse emission near the cloud is assumed to be not associated with it. It was subtracted by defining two reference regions along the cloud's north and south edges, and then using the I, Q, and U measurements in these regions to fit a linear emission profile, which was then subtracted. The use of the two reference regions effectively defines a "validity area" between them (cyan box in Figure 1).

Finally, following Fissel et al. (2016), we proceed under the assumption that the most suitable diffuse emission subtraction method probably corresponds to an intermediate version, lying between the aggressive and conservative methods. Accordingly, an "intermediate" diffuse emission subtraction method is introduced, which involves averaging the respective I, Q, and U maps corresponding to the two extreme methods. In this work, unless otherwise explicitly stated, all results and analysis employ intermediate diffuse emission subtraction. However, our final analysis of the polarization efficiency ratio (Section 5.3) takes into account the systematic uncertainties associated with the diffuse emission subtraction process.

2.4. Data Selections Applied to BLASTPol and I-band Polarization Measurements

Similarly to the procedure adopted by Fissel et al. (2016), we select for analysis only the data that do not present strong variations between the results obtained from the various diffuse subtraction methods. Representing polarization degrees and position angles for the intermediate, conservative, and aggressive diffuse emission subtraction methods respectively as ($p_{\rm int}$, $\phi_{\rm int}$), ($p_{\rm con}$, $\phi_{\rm con}$), and ($p_{\rm agg}$, $\phi_{\rm agg}$), we require that $p_{\rm int} > 3|p_{\rm int} - p_{\rm agg}|$ and $p_{\rm int} > 3|p_{\rm int} - p_{\rm con}|$, and also that $|\phi_{\rm int} - \phi_{\rm agg}| < 10^\circ$ and $|\phi_{\rm int} - \phi_{\rm con}| < 10^\circ$. Finally, for both the I-band and BLASTPol data sets, we require that the S/N in the polarization fraction satisfies $p/\sigma_p > 3$, completing the definitions of the basic BLASTPol and basic I-band data sets (Table 1). After applying these selection criteria, 6740 stars remain in the basic I-band data set.

3. Consistency between Submillimeter and Near-IR Magnetic Field Angles

3.1. Combined Polarization Map

Figure 2 shows the combined polarization map, in which cyan pseudovectors represent I-band observations and red pseudovectors are the 500 μm polarimetric measurements (rotated by 90° in order to match with the orientation of the sky-projected magnetic field), using the basic data sets in both cases. Pseudovector lengths are proportional to polarization degree. The background image (see also Figure 1) is a map of hydrogen column density estimated from *Herschel* dust emission data (see Section 4.3). The *Herschel* data also provide an estimate of the cloud visual extinction levels, as shown by the inner ($A_V = 25$ mag, dark green) and outer ($A_V = 10$ mag, light green) contours in Figure 2.

I-band pseudovectors surround the denser portions of the cloud, tracing the more diffuse molecular material, with far fewer detections at $A_V > 10$ mag (in this work we will generally limit the analysis to cloud extinction levels below 20 mag). An exception occurs in the vicinity of the RCW 36 HII region, as indicated by a white circle (10′ radius). Here the presence of bright OB-type stars in the star-forming cluster (Baba et al. 2004) allowed many I-band polarization detections even at higher extinction levels. Good-quality submillimeter detections, on the other hand, are mainly found in the denser regions of the cloud (see Section 3.2), where higher fluxes give better sensitivity. Large areas of overlap between submillimeter and near-IR pseudovectors are seen in Figure 2. These areas are used to define the "basic polarization combination" data set (see Table 1). We select submillimeter polarization values corresponding to each stellar position, using a finely gridded BLASTPol map with 10″ pixel size. The basic polarization combination data set is composed of 1355 individual lines of sight containing both submillimeter and I-band data. However, before correlating polarization data from extinction and emission directly, a careful selection of the suitable stars for this comparison needs to be done, as discussed in the next sections.

3.2. Agreement between Magnetic Field Orientation and Exclusion of the RCW 36 Region

As discussed in detail in Section 4, the main challenge to be dealt with before directly comparing polarization from emission and extinction is to make sure both methods are probing the same interstellar material along the LOS. The polarized emission data trace only the molecular cloud (see Section 2.3), while polarization from stars, which are distributed in a range of distances along the LOS (see Appendix A), could be contaminated by the foreground/background material. A first step is to select data for which respective polarization angles from the two data sets agree, thereby ensuring that the set of sky-projected magnetic field orientations sampled along the LOS coincides. This procedure could exclude, for example, stars in the foreground or far away in the background, tracing magnetic field structures not associated with the cloud itself. Note, however, that if there are no strong changes in field orientation along the LOS, similar angles will be found even when probing different columns of interstellar material (e.g., see discussion in Section 4). Therefore, the angle requirement is necessary but not sufficient.

Figure 2 allows a visual comparison of the sky-projected magnetic field lines traced by the two data sets, showing good agreement over most of the map. Representing the I-band and 500 μm magnetic field angles respectively as θ_I and θ_{500}, in Figure 3 we show a histogram of the difference $\Delta\theta = \theta_I - \theta_{500}$ (top) as well as a map where the color scale represents the absolute value of those differences (bottom). The distribution is closely centered near $\Delta\theta = 0^\circ$ (the Gaussian fit is peaked at 2.°0 with a standard deviation of 12°). Since background stars at different distances map different interstellar background components, one might expect a large discrepancy when

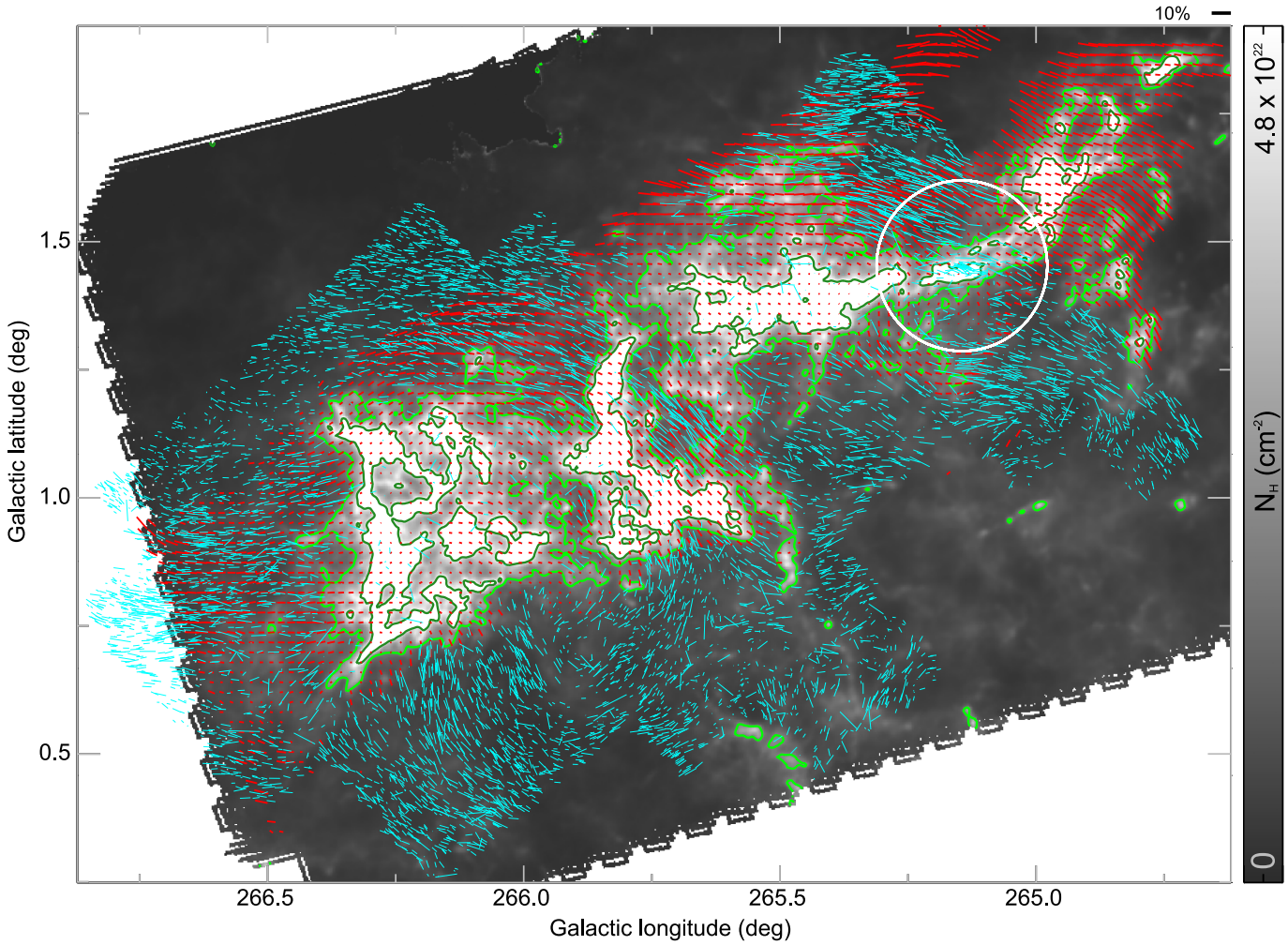

Figure 2. Polarization map of Vela C, including both the *I*-band (cyan) and the BLASTPol (red, rotated 90°) basic data sets as defined in Table 1. The background image is described in Section 3.1 and is the same as shown in Figure 1. It shows column density ($N_{\rm H}$), with outer and inner contours representing visual extinction levels of 10 (light green) and 25 mag (dark green), respectively. The sizes of pseudovectors are proportional to the polarization degree, with a reference 10% pseudovector shown at the top right. The white circle has 10′ radius and is centered on RCW 36.

comparing near-IR and submillimeter polarization angles. The good correlation seen in Figure 3 suggests that among all interstellar components along the LOS, the Vela C cloud itself has a dominant effect in determining the polarization angle. Nevertheless, to be prudent, we will restrict our sample to $\Delta\theta < 15°$, which corresponds approximately to half of the distribution's FWHM. This criterion removes the outliers for which the two data sets could be probing different interstellar components. This is a conservative choice, given that even if no restriction to $\Delta\theta$ is applied, although the number of data samples available for the analysis increases slightly, it does not significantly affect the final results that are presented in Sections 5.3 and 5.4.

BLASTPol data from the RCW 36 area suffer from systematic uncertainties that are typically larger than the statistical errors. Null tests carried out by Fissel et al. (2016) show significant structures around RCW 36 in the residual Q and U maps. Furthermore, analyzing the map in Figure 3, we notice that around RCW 36 (white circle) $\Delta\theta$ is systematically higher. Since it is known that many of the stars detected in that area are part of the star-forming cluster in the HII region (Baba et al. 2004) and therefore embedded in the cloud, we believe that the discrepancy might be explained as follows: while the 500 μm polarization integrates the emission along the entire cloud, the near-IR pseudovectors trace magnetic fields only up to the position of the corresponding embedded star. In view of this possibility, we adopt a conservative approach by excluding all stars located inside the white circle.

4. The Stellar Distance Problem and A_V Estimates

As described in Section 2.3, after subtraction of the foreground/background contribution, the polarized emission data trace only the molecular cloud. Therefore, the stars with *I*-band polarization data that are suitable for comparison with polarized emission data are the ones immediately behind the molecular cloud, in the near background. The situation is illustrated in Figure 4. The important issue is that stars detected via our near-IR polarimetry observations are distributed at a range of distances in the cloud's LOS, but only a small subset of objects located in the near background of the cloud should be selected, avoiding the inclusion of foreground stars and also far-background stars contaminated by material from the Galactic disk. For the purpose of adopting a clear nomenclature, near-background objects are henceforth referred to as "ideal" stars, and objects

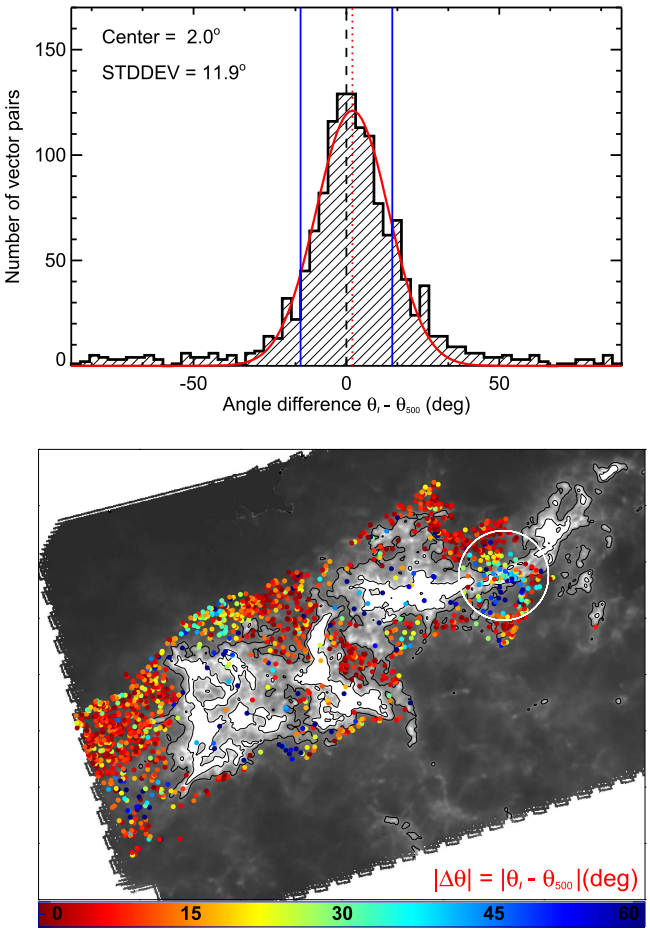

Figure 3. Top: histogram of the difference in magnetic field orientation between the *I*-band and 500 μm data from the basic polarization combination data set of 1355 stars (see Table 1). The red curve represents a Gaussian fit to the distribution (its center and standard deviation are specified in the figure). Vertical blue lines represent the $\Delta\theta < 15°$ data cut (see Section 3.2). Bottom: estimated column density map of Vela C (same as shown in Figure 1), with colored dots representing the absolute value of the magnetic field angle difference ($|\Delta\theta| = |\theta_I - \theta_{500\mu m}|$). The white circle is centered on RCW 36.

located sufficiently far away in the background (so that the additive extinction from the diffuse Galactic ISM is nonnegligible) are referred to as "far-background" stars (see Figure 4).

4.1. The Basic Method for Choosing Near-background Stars

Since individual stellar distances are typically not known through photometric or trigonometric parallax techniques, we will identify ideal stars by analyzing the distribution of stellar visual extinctions (A_V^{st}), as illustrated in Figure 4. Considering a specific LOS in the direction of the cloud, the distribution will typically exhibit a distinguishable population of foreground stars with low extinctions, illustrated in Figure 4 as a low-A_V peak. As we move to larger distances going through the cloud, near-background (ideal) stars will have higher extinctions, therefore defining a rise in the distribution. Continuing to even larger distances, far-background stars might have additional extinction from some background material in the Galactic disk. Therefore, stars located at the rise in the distribution (after the "gap" located just beyond the foreground stars) should be ideal

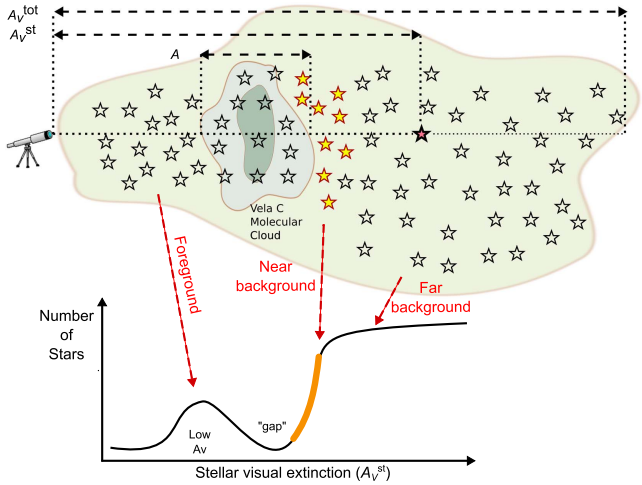

Figure 4. Schematic image showing the distribution of stellar objects in the direction of Vela C, consisting of foreground, embedded, near-background (here called ideal; yellow), and far-background stars. The expected distribution of stellar extinctions is also shown (bottom); this includes a Gaussian-like population of foreground stars at low extinctions and a steep rise corresponding to objects located in the near background (ideal stars). For the LOS of a particular example object (denoted by the red star), three types of extinction measurements are defined (top). These are the stellar extinction A_V^{st}, the cloud extinction A_V^{cl}, and the total LOS extinction A_V^{tot}.

stars that are suitable for use in computing the polarization efficiency ratio.

In order to carry out the analysis described above, first it is necessary to define three different types of visual extinction measurement (see Figure 4): (1) the stellar extinction, A_V^{st}, defined by the column of material extending as far as the stellar location, which can be estimated through near-IR photometry; (2) the cloud visual extinction, A_V^{cl}, which accounts only for the molecular cloud column, therefore being foreground and background subtracted; and (3) a visual extinction accounting for the entire column of interstellar material along the LOS, defined as A_V^{tot}. In Sections 4.2–4.4 we describe how these three types of visual extinction measurement are determined. These measurements will subsequently be used to select ideal stars.

4.2. Determining Stellar Visual Extinction (A_V^{st}) from 2MASS

Even considering that the individual spectral types for each object are not known, an approximate estimate of A_V^{st} may be obtained using the stars' $J - H$ and $H - K_s$ colors from the 2MASS catalog (Skrutskie et al. 2006). This method has been used, for example, by Whittet et al. (2008) in their analysis of optical polarization efficiencies (p/A_V) in the Taurus and Ophiuchus dark clouds. Each observed star defines a position in a color–color diagram (Figure 5, top), and the color excess values ($E(J - H)$ and $E(H - K_s)$) may be obtained through extrapolation along the reddening band (black dashed lines) onto the intrinsic color lines[24] (superposed solid red lines). The method discussed here was applied to all objects located within both the blue box of Figure 1 and the boundaries of the *Herschel* map. We define this sample as the "wide photometric field" (Table 1). It encompasses most stars with *I*-band

[24] Intrinsic colors are obtained from Koornneef (1983) and further corrected to the 2MASS photometric system through transformation relations provided by Carpenter (2001).

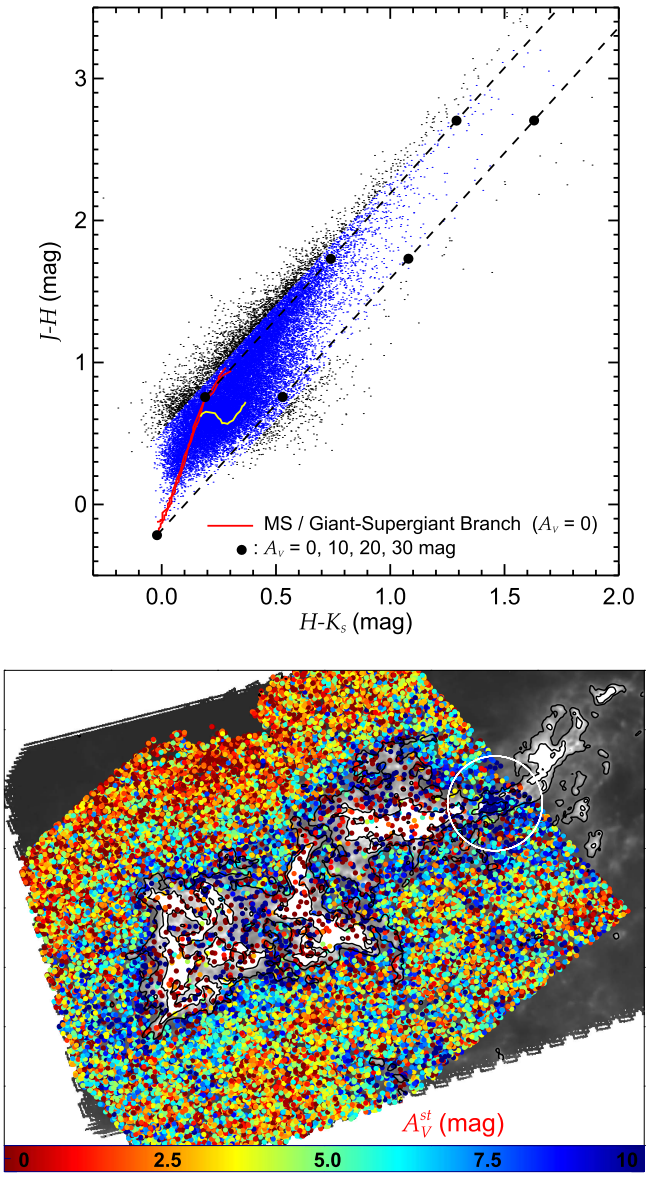

Figure 5. Top: color–color diagram ($J - H$ vs. $H - K_s$) for 2MASS stars in the wide photometric field (see Section 4.2 and Table 1). Stellar extinctions (A_V^{st}) are estimated for all objects located inside the reddening band (the area between the parallel black dashed lines). Here, A_V^{st} is proportional to the distance between the object and the main-sequence/giant locus (the red lines at the bottom left). Objects outside and inside the reddening band are shown as black and blue points, respectively. The yellow line corresponds to the locus of main-sequence stars with spectral types later than K7. Bottom: estimated column density map of Vela C (same as shown in Figure 1), with colored dots overlaid representing stellar extinctions A_V^{st} for 2MASS stars in the wide photometric field. The white circle is centered on RCW 36.

polarimetric detections, in addition to a vast sample of the stellar population in the direction of Vela C. This wider set of photometric data will be useful for the analysis of Sections 4.5 and 5.2.

Martin et al. (2012) showed that for the ISM around Vela C, the slope of the reddening band is 1.77 ± 0.01, which is evident here in the elongated distribution of points along the black dashed lines in Figure 5. Dereddening each point along the reddening band generally provides unambiguous results, since the main-sequence, giant, and supergiant loci all correspond to superposed lines in this diagram, except for a subset of late-type main-sequence stars (the yellow line in Figure 5). However, taking into account the 2MASS photometric completeness limits in the J, H, and K_s bands, it is straightforward to show that at distances of 700 pc or greater, main-sequence stars with spectral types later than approximately K7 would not be bright enough to be detected, and therefore the portion of the main sequence indicated by a thin yellow line may be ignored (foreground objects are an obvious exception, but these will be removed from the analysis later; see Section 5.2).

The conversion from color excess to visual extinction can be carried out in several different ways. For instance, canonical relations can be obtained from Rieke & Lebofsky (1985) or Fitzpatrick (1999), provided that some value for the total-to-selective extinction is adopted. Another option is to take advantage of the updated relation between $E(J - K_s)$ and total hydrogen column density $N_{\rm H}$ obtained by Martin et al. (2012, Equation (9)) by reassessing previously published ultraviolet stellar spectroscopic data and comparing it with 2MASS data. Since in the present work we are using the same catalog of near-IR photometry (2MASS) as was used by Martin et al. (2012), this last method seems most appropriate. By using it, we avoid any conversion errors due to mismatch in the photometric system employed. We obtain $E(J - K_s)$ for each star by summing $E(J - H)$ and $E(H - K_s)$. Then, we combine Equation (9) from Martin et al. (2012) (which relates $E(J - K_s)$ to $N_{\rm H}$) with the gas-to-dust relation $N_{\rm H} = 1.9 \times 10^{21}$ cm$^{-2} A_V^{\rm st}$ (Savage et al. 1977; Bohlin et al. 1978; Rachford et al. 2009). The resulting relation between $E(J - K_s)$ and $A_V^{\rm st}$ is

$$A_V^{\rm st} = 6.05 E(J - K_s) - 0.04. \quad (1)$$

It is important to point out that the above-mentioned gas-to-dust relation includes the assumption that $A_V = 3.1 E(B - V)$ (e.g., Draine 2003) and that the total-to-selective extinction ratio depends on grain properties, thus providing a source of systematic uncertainties (see discussion at the end of this subsection).

To define the wide photometric field sample, we keep only stars with 2MASS photometric quality "AAA," signifying a photometric detection with S/N > 10 and uncertainties in J, H, and K_s below 0.1 mag. Furthermore, stars located well outside the reddening band (black dots in Figure 5, top) are excluded in order to avoid extragalactic sources and young stars with circumstellar disks, which are known to exhibit infrared excess and sometimes intrinsic polarization.

The distribution of stellar extinctions $A_V^{\rm st}$ is shown in the bottom panel of Figure 5. Note that closer to the cloud the average extinctions are generally higher. Also note that many stars with very low extinctions may be found within the cloud contours, and objects with high extinctions may be found well off the cloud. These objects have properties consistent with being, respectively, foreground and far-background stars. In Section 4.5 and Appendix A we show that the wide distribution of $A_V^{\rm st}$ values seen for off-cloud positions is primarily due to distance, with stars located at large distances behind the cloud having higher extinctions due to the presence of diffuse ISM in the far background.

4.3. Determining Cloud Visual Extinction (A_V^{cl}) from Herschel

The foreground and background subtracted molecular cloud extinction A_V^{cl} was estimated from dust emission maps made by *Herschel* SPIRE at 250, 350, and 500 μm. The technique used is similar though not identical to the one described by Fissel et al. (2016). One difference is that we did not smooth the *Herschel* maps to the BLASTPol resolution. Another difference is that we did not make use of the 160 μm PACS map, since it covers a smaller sky area in comparison with the SPIRE maps. In brief, the technique consists of, first, using previously selected "diffuse emission regions" surrounding the cloud (containing little or no emission from the cloud itself) to calculate the diffuse Galactic contribution for each waveband. These are then subtracted from each corresponding SPIRE map. Modified blackbody SED fits were then constructed for each pixel, assuming the dust opacity law of Hildebrand (1983) with a dust spectral index of $\beta = 2$, thus generating column density ($N_{\rm H}$) and temperature maps (T). Finally, the relation $N_{\rm H} = 1.9 \times 10^{21}$ cm^{-2} A_V^{cl} was used to obtain the cloud extinction map. It is important to point out that the assumptions used above are strictly valid only for diffuse lines of sight. There is evidence in the literature that the submillimeter optical depth per unit column density increases somewhat for higher density molecular clouds due to grain processing (Planck Collaboration XXV 2011), leading to some uncertainty.

As previously mentioned, A_V^{cl} contours corresponding to 10 and 25 mag are shown in Figure 2. Note that for sky regions covered by the 160 μm maps, we found very little difference between A_V^{cl} values derived with and without the 160 μm data.

4.4. Determining Total Visual Extinction for the Entire LOS (A_V^{tot}) from Planck

In order to obtain the visual extinction for the entire LOS corresponding to each individual star in our sample, including the entire column up to and beyond the star, we use the 353 GHz optical depth from *Planck* all-sky mapping. Planck Collaboration XI (2014) correlated their 353 GHz optical depth (τ_{353}) with estimates of color excess $E(B-V)$ for quasars, based on photometric measurements from the Sloan Digital Sky Survey. Using extragalactic objects rather than Galactic stars ensured that the entire Galactic column in the direction of each quasar was probed, avoiding biases that could arise from background contamination. They found $E(B-V)/\tau_{353} = (1.49 \pm 0.03) \times 10^4$ mag. By assuming that $A_V = 3.1E(B-V)$, we converted the *Planck*-derived selective extinction measurements to A_V^{tot}.

4.5. Comparisons between A_V^{st}, A_V^{cl}, and A_V^{tot}

A comparison between A_V^{st} and A_V^{cl} is shown in Figure 6 (top). This diagram includes all of the stars from the wide photometric field (Section 4.2 and Table 1). Note that most of the points are located somewhat above the equality line (dashed red line), which suggests that many of these objects are affected by extinction from the background ISM. In Appendix A we consider Galactic models for stellar and dust distribution together with the sensitivity of the 2MASS survey, and we conclude that the wide photometric field is expected to include large numbers of stars located in the far background (≈2–10 kpc), behind several magnitudes of additional extinction caused by diffuse Galactic ISM behind the cloud. Although several other factors may affect comparisons between

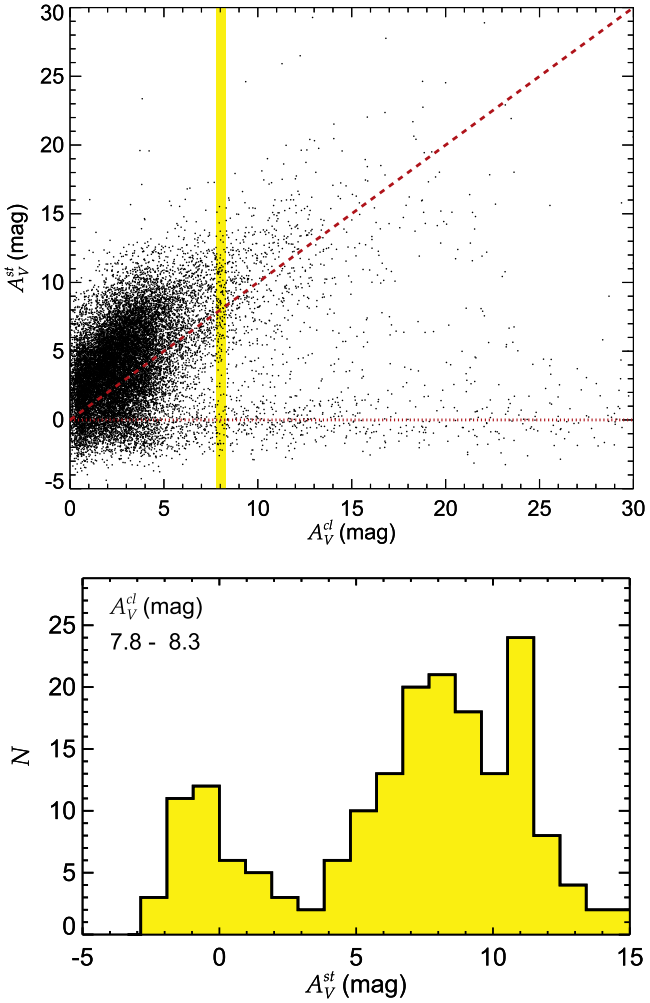

Figure 6. Top: diagram comparing stellar extinctions (A_V^{st}) and cloud extinctions (A_V^{cl}) for objects located within the wide photometric field (see Table 1). Dashed and dotted lines representing the equalities $A_V^{st} = A_V^{cl}$ and $A_V^{st} = 0$, respectively, are shown for reference. Bottom: example A_V^{st} histogram for a bin of A_V^{cl} centered on $A_V^{cl} = 8$ mag (corresponding to the yellow vertical band in the top panel), showing the gap between the foreground and background stellar extinction distributions.

A_V^{st} and A_V^{cl} (Appendix A), the primary cause for the wide spread of points above the equality line is this population of far-background stars contaminated by background extinction. For a fixed A_V^{cl} value, one can see that there is a population of foreground objects near $A_V^{st} = 0$ (dotted line). As one moves farther up in stellar extinction A_V^{st}, a "gap" region is found, followed by a rise in the number of stars. For example, for $A_V^{cl} \approx 8$ mag (vertical yellow band in Figure 6, top), we see a cluster of points near $A_V^{st} = 0$, another cluster around A_V^{st} =6–12 mag, and very few points in the "gap" near A_V^{st} =2–4 mag. This can be seen in Figure 6 (bottom), which is a histogram of A_V^{st} for a small A_V^{cl} bin centered on $A_V^{cl} = 8$ mag. The histogram clearly exhibits a gap between the foreground and background stellar populations. This is consistent with the expectation described above (Figure 4, Section 4.1).

We have argued that many stars are contaminated by a background Galactic extinction component (and therefore are located farther away from the cloud, in the far background). An independent way of testing this is to compare with visual

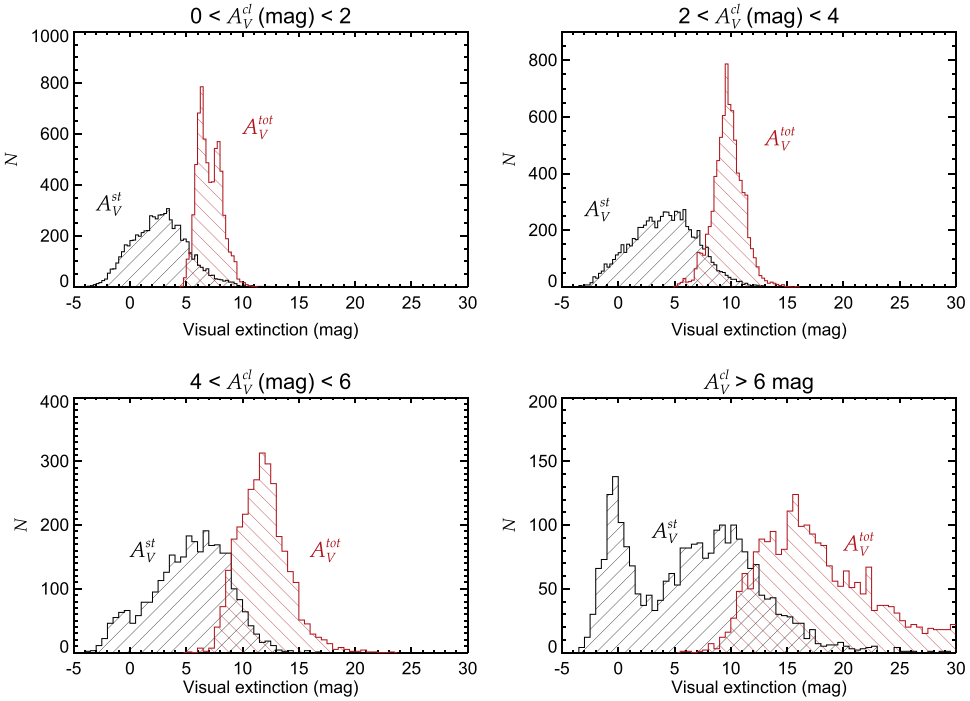

Figure 7. Histograms of stellar extinction $A_V^{\rm st}$ and total LOS extinction $A_V^{\rm tot}$ for different ranges of cloud extinction $A_V^{\rm cl}$, including all objects from the *Planck*–2MASS combination data set (see Table 1).

extinction estimates that account for the entire LOS ($A_V^{\rm tot}$), using the *Planck*–2MASS combination data set (see Table 1). Figure 7 shows visual extinction histograms for different $A_V^{\rm cl}$ ranges, including the distributions for both $A_V^{\rm st}$ (black) and $A_V^{\rm tot}$ (red). It is clear that regardless of which depth through the cloud one uses (i.e., for all $A_V^{\rm cl}$ ranges), the $A_V^{\rm tot}$ distribution always extends to higher levels than $A_V^{\rm st}$. In particular, that is true even when the contribution from the cloud itself is small (see the first histogram of Figure 7, for which $0 < A_V^{\rm cl} < 2$ mag). This histogram shows that even for the relatively diffuse areas surrounding the cloud, the visual extinction integrated along the entire LOS is typically between 5 and 10 mag, while stellar extinctions have a broader distribution, but centered at ≈3 mag.

Our analysis of Figure 7 supports the existence of a significant column density of background ISM. This hypothesis is also consistent with the distribution of points in Figure 6 (top), and with the analysis of Appendix A, as noted earlier. We conclude that many stellar objects are contaminated by background ISM and will have to be removed from the sample. Appendix B shows an independent set of evidence for the existence of this contaminating far-background material, based on a separate analysis of stellar extinction as a function of distance.

5. Computing the Polarization Efficiency Ratio $R_{\rm eff}$

5.1. Foreground Correction for Stellar Extinction and Polarization

Our qualitative analysis of Figure 6 (top) revealed that there is a group of stars forming a "band" approximately following the line $A_V^{\rm st} = 0$ mag (red dotted line). For these stars, independent of the cloud's extinction along the LOS, stellar extinctions are very low. This is a characteristic feature of foreground stars. Such stars must be removed from this analysis. Furthermore, it is expected that diffuse material in front of the Vela C cloud contributes a small fraction of the extinction measured for background stars (although the $A_V^{\rm st}$ values derived from 2MASS do not provide the necessary sensitivity to estimate this small component). Additionally, a foreground polarization is also imposed on the stellar light from background stars. Both the extinction and polarization components originating from the foreground ISM must be subtracted.

Estimates of the foreground extinction and polarization in the direction of Vela C are obtained in Appendix C. We find that the foreground ISM toward Vela C is in general very diffuse, with an extinction level of approximately 0.15 ± 0.09 mag. For the purposes of defining the corrected polarization combination data set that will be used in the analysis of Section 5.3 (see also Table 1), this foreground extinction value is subtracted from $A_V^{\rm st}$, and additionally, only stars with $A_V^{\rm st}/\sigma A_V^{\rm st} > 3$ are used (where $\sigma A_V^{\rm st}$ are the statistical uncertainties derived from propagation of 2MASS photometric errors). The foreground polarization is estimated as $p_I = 0.4\%$ and $\theta_I = 132°$. This component is subtracted from the measured polarization values of our sample, using standard techniques (e.g., Santos et al. 2014), and then we reapply the $p_I/\sigma_{pI} > 3$ criterion. These selections complete the definition of the corrected polarization combination data set as specified in Table 1 (where we also summarize all of the additional selection criteria described in Sections 2.4, 3.2, and 4.2).

5.2. The Gaussian-logistic Method of Selecting Ideal Stars

As discussed in Section 4.1 above, only ideal stars (located in the near background) are suitable for a quantitative comparison between polarization data sets obtained from

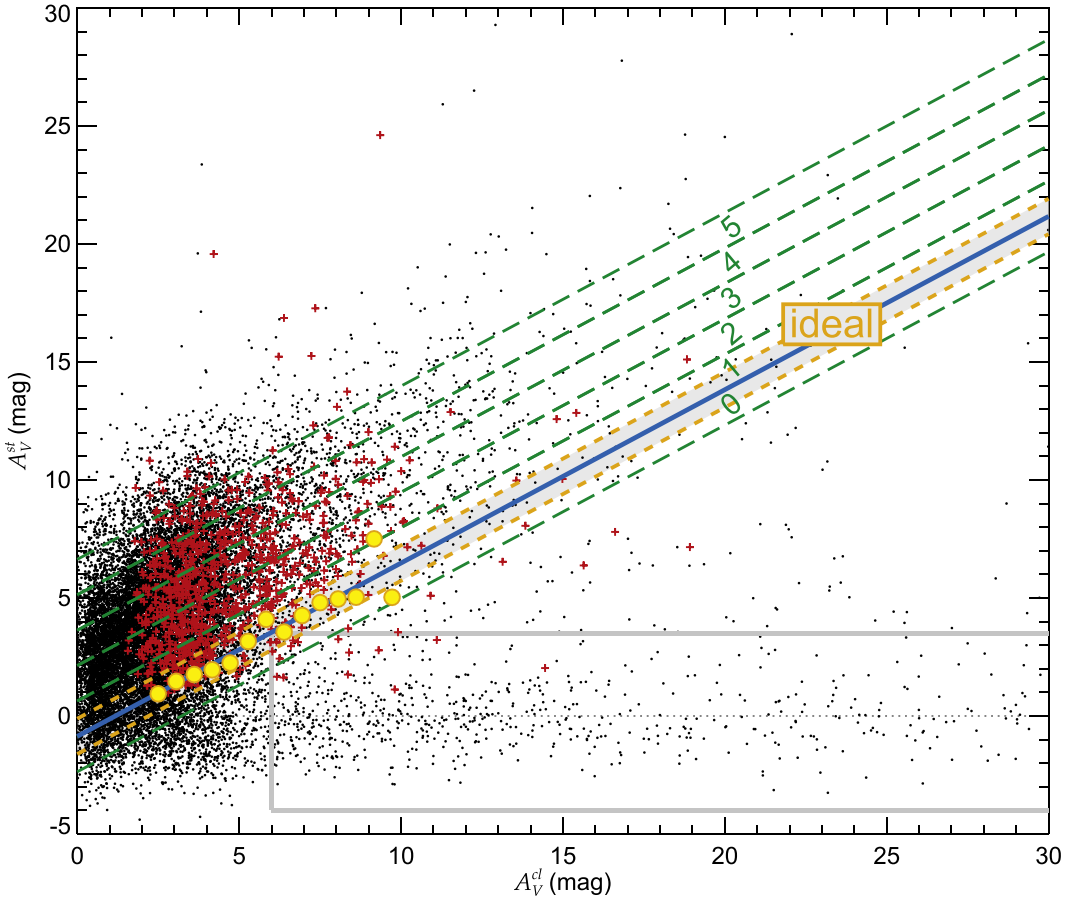

Figure 8. Stellar extinctions $A_V^{\rm st}$ vs. cloud extinction $A_V^{\rm cl}$ for stars in the wide photometric field data set (black dots), and stars in the corrected polarization combination data set (red crosses). Data sets are defined in Table 1. The gray box is used to define the $A_V^{\rm st}$ distribution of foreground stars as an input to the GL method, and the yellow circles are the midpoints A_V^0 of the logistic function for different $A_V^{\rm cl}$ bins, obtained as outputs from the same method (see Section 5.2 and Appendix D). The blue line is a fit to the yellow circles and allows us to define the "ideal stellar sample" (points in the grayed area between the two dashed orange lines), which is the set of objects located in the near background (Section 5.2). Strips 0–5 (bounded by the green lines) are defined parallel to the ideal stellar locus and are used to study the effects of background contamination (see Sections 5.2 and 6.3).

extinction and emission. Notice that these objects cannot be selected without bias simply through a direct comparison such as $A_V^{\rm st} = A_V^{\rm cl}$, because of the uncertainties associated with the derivation of $A_V^{\rm cl}$ from *Herschel* data (see Section 4.3). Instead, we apply an empirical method that does not rely on a direct comparison between $A_V^{\rm st}$ and $A_V^{\rm cl}$. Figure 4 shows a schematic profile of the stellar extinction distribution expected toward a given LOS, composed of a foreground population at low extinction, followed by a steep rise in the number of stars, corresponding to the "ideal" stars. Furthermore, we observed this expected profile in the data from the wide photometric field (Figure 6). Accordingly, we model the $A_V^{\rm st}$ distribution within different bins of cloud extinction $A_V^{\rm cl}$ using a Gaussian-logistic (GL) function, defined as a Gaussian function added to a logistic profile (which can be described as a smoothed step function):

$$N^{\rm st}(A_V^{\rm st}) = \alpha e^{\frac{(A_V^{\rm st}-\beta)^2}{2\sigma^2}} + \frac{a}{1+e^{-b(A_V^{\rm st}-A_V^0)}}. \quad (2)$$

In this equation, $N^{\rm st}$ is the number of stars (within a certain bin of cloud extinctions $A_V^{\rm cl}$), given as a function of the stellar extinction $A_V^{\rm st}$. In the first term, which represents the foreground stellar population, parameters α, β, and σ are the height, displacement, and width (the standard deviation) of the Gaussian fit, respectively. In the second term, which represents the background stellar population, parameters a, b, and A_V^0 represent the height of the logistic function, its steepness, and the midpoint of the logistic curve, respectively.

To specify the subsets of the data that are used in the GL fits, in Figure 8 we show again the comparison between stellar and cloud extinction. The black dots represent the wide photometric field sample, identical to what is shown in Figure 6 (top). The GL method does not require any polarization measurements and therefore should be applied to the maximum number of stars available. For this reason, we apply it to the wide photometric field. After the application of the GL method, however, stars that will be available for the computation of the polarization efficiency ratio are only those in the corrected polarization combination data set (containing both *I*-band and 500 μm polarization data; see Table 1). These are indicated in Figure 8 by the red crosses; a subset of these stars selected as ideal objects via the GL method will be used to compute the polarization efficiency ratio.

A detailed description of the GL method is given in Appendix D. The basic idea is to fit Equation (2) to different

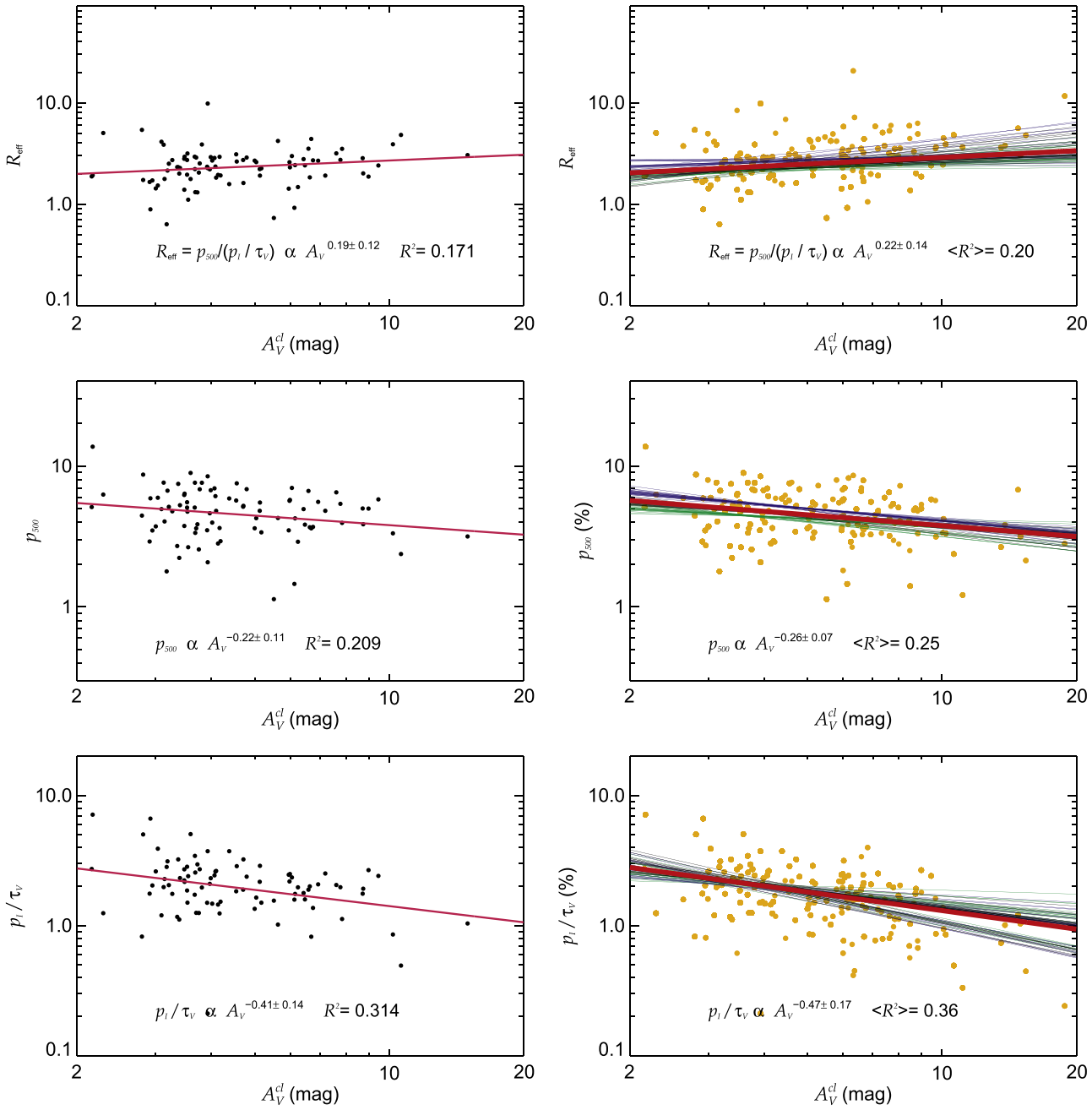

Figure 9. Diagrams of $R_{\rm eff}$ vs. $A_V^{\rm cl}$ (top, the polarization efficiency ratio $p_{500}/(p_I/\tau_V)$ as a function of cloud extinction), p_{500} vs. $A_V^{\rm cl}$ (middle), and p_I/τ_V vs. $A_V^{\rm cl}$ (bottom), using only the ideal stellar sample in each case. The ideal stellar sample is selected using the GL method. Diagrams on the left are for the standard example. Power-law fits are shown in each case, together with Pearson correlation coefficients (R^2). Diagrams on the right account for systematic uncertainties through a series of variations of the GL method input parameters ($N_{\rm d}$, $R_{\rm bin}$, and $N_{\rm max}$), resulting in slightly different ideal stellar loci and consequently different fitted curves. The differences between diffuse emission subtraction methods are also accounted for; black, blue, and green curves are, respectively, for intermediate, aggressive, and conservative subtraction methods. The red curves are obtained by taking the mean (and standard deviation) of the individual power-law exponents for the various individual fitted curves shown. Orange dots represent the "extended" ideal stellar sample, showing only the points for the intermediate diffuse subtraction method. Details are given in Section 5.3 and Appendix D.

distributions representing different bins of $A_V^{\rm cl}$ (one can imagine this as a series of vertical slices in Figure 8; see also Figure 6). The important quantity here is A_V^0, which represents the position of the rise in the number of stars (the midpoint of the logistic function) and therefore defines the locus of ideal stars for each bin of cloud extinctions. In Figure 8, the yellow circles show the position of A_V^0 for each $A_V^{\rm cl}$ bin (using the center of each bin). These points are fit to a straight line (the blue line), which represents the positions where ideal stars are found. We define a series of "strips" parallel to this line, labeled from 0 to 5 (delimited by green dashed lines), and a special strip defined as the "ideal stellar locus" (grayed area between the orange dashed lines). In the figure, strip 0 is below the ideal stellar locus, and higher strips represent increasingly distant far-background stars whose $A_V^{\rm st}$ values (and I-band polarization) are increasingly contaminated by the Galactic ISM. Red crosses inside the ideal locus define the "ideal stellar sample" (Table 1), which

will be used to compute the polarization efficiency ratio. The vertical separation between consecutive strips is 1.5 mag, which is on the order of the typical uncertainty in $A_V^{\rm st}$ (see Appendix C). Since the separation between lower and higher strips is larger than the typical $A_V^{\rm st}$ uncertainties, we expect that higher-numbered strips will clearly show increasing levels of background contamination in their measured *I*-band polarizations. We return to this point in Section 6.3.

5.3. Polarization Efficiency Ratio and Analysis of Systematic Uncertainties

Having determined the locus of ideal stars in the $A_V^{\rm st}$ versus $A_V^{\rm cl}$ diagram, we are now in a position to study the polarization efficiency ratio ($R_{\rm eff}$). We will refer to the method of data analysis described in this subsection as the "standard analysis" of polarization properties. Here, $R_{\rm eff}$ is defined as the ratio between polarization fraction at 500 μm (p_{500}) and polarization efficiency in the *I* band, p_I/τ_V (where $\tau_V = A_V^{\rm st}/1.086$ is the optical depth):

$$R_{\rm eff} = \frac{p_{500}}{p_I/\tau_V}. \quad (3)$$

In order to understand how the various relevant quantities vary as we move toward higher cloud depths, in Figure 9 (left) we show $R_{\rm eff}$, p_{500}, and p_I/τ_V, respectively, as a function of $A_V^{\rm cl}$, using only objects from the ideal stellar sample (Table 1). For each of these profiles, we also fit a power law (red curve), together with a calculation of R^2, the Pearson correlation coefficient. All points are given equal weight, and the fits are limited to the range 2 mag $< A_V^{\rm cl} <$ 20 mag, where most of the data are distributed.

Although curves in Figure 9 (left) might seem sufficient to analyze the polarization efficiency ratio and its dependence on $A_V^{\rm cl}$, the analysis is affected by systematic uncertainties that depend on the various choices of input parameters for the GL method and also on the choice of diffuse emission subtraction method (Section 2.3). The example shown in Figure 9 (left) corresponds to a single choice of input parameters, which we refer to as the "standard example" (see Appendix D). As described in Section 2.3, three alternate types of diffuse emission subtraction were used (conservative, aggressive, and intermediate). The choice of method affects the calculation of $R_{\rm eff}$, and the resulting uncertainty should be accounted for in the analysis. A detailed description of our treatment of these systematic uncertainties is given in Appendix D. Basically, the GL method is reapplied a number of times, in each case varying a set of input parameters that slightly change the resulting locus of ideal stars. Using slightly different ideal stellar loci in turn changes the resulting parameters of the power-law fits. The diffuse emission subtraction method is also varied.

The results are shown in Figure 9 (right), in which each curve is obtained using the ideal stellar sample that corresponds to one particular parameter set, with black, blue, and green curves corresponding to intermediate, aggressive, and conservative diffuse emission subtraction, respectively. Identically to Figure 9 (left), we show $R_{\rm eff}$, $p_{500\mu{\rm m}}$, and p_I/τ_V as a function of $A_V^{\rm cl}$. The points in these diagrams (orange dots) show all stars that were found inside the ideal stellar locus at least once. We define this combination of points as the "extended" ideal stellar sample. The power-law exponents (and errors) shown in each panel are the averages (and standard deviations) of the set

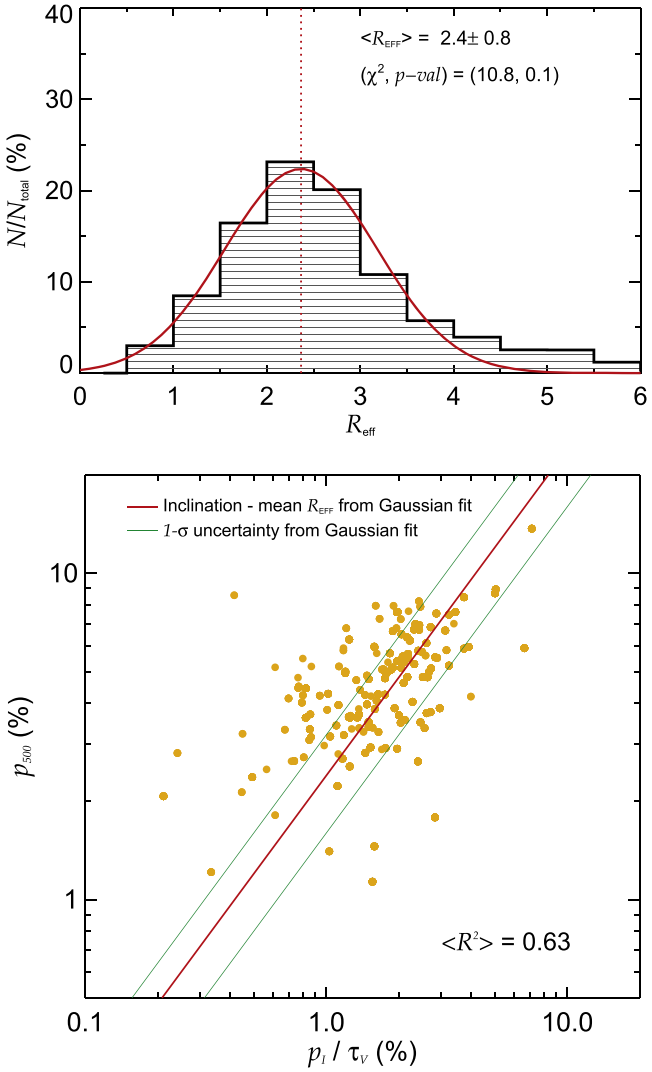

Figure 10. Normalized histogram of the polarization efficiency ratio $R_{\rm eff} = p_{500}/(p_I/\tau_V)$ (top) and a direct comparison between p_{500} and p_I/τ_V (bottom). Both diagrams include objects from the "extended" ideal stellar sample, but the bottom one is showing only points for the intermediate diffuse emission subtraction method. The Gaussian fit to the $R_{\rm eff}$ histogram gives a best estimate of $R_{\rm eff} = 2.4 \pm 0.8$. The chi-squared ($\chi^2$) and associated *p* value for the Gaussian fit are also shown. The positions of the red and green lines in the bottom diagram represent this best value estimate and its uncertainty, respectively, as obtained from the Gaussian fit in the top panel (these lines are not obtained from a linear fit; see Section 5.4).

of exponents obtained for the various individual fits corresponding to the various choices of input parameters and diffuse emission subtraction method. The same procedure is applied to obtain the displayed correlation coefficients. Using the average exponent values, we draw the average curve (red), which may be viewed as the best solution, with an uncertainty represented by the range of individual curves. Notice that for each of the three plots on the right side of Figure 9, the dispersion in the fitted exponents (the standard deviation) is similar to the statistical uncertainty in the power-law exponents obtained using the standard example fit (left panels).

The GL method was applied in order to avoid including far-background stars whose polarization measurements are significantly contaminated by the interstellar material of the Galactic disk. For completeness, it is also instructive to understand the effect of including far-background objects, by

applying the "standard analysis" of polarimetric properties to all strips defined in Figure 8. Section 6.3 shows the results of this analysis and provides further discussion on background contamination.

5.4. Determination of the Mean Polarization Efficiency Ratio $R_{\rm eff}$ in the $2 < A_V < 20$ mag Range

The $R_{\rm eff}$ versus $A_V^{\rm cl}$ curve shown in Figure 9 (top right) has a positive slope, with a power-law exponent given by 0.22 ± 0.14. The correlation coefficient is low ($\langle R^2 \rangle = 0.20$). Nominally, our best estimate for the power-law exponent implies $R_{\rm eff}(20\ {\rm mag})/R_{\rm eff}(2\ {\rm mag}) = 1.7$, where $R_{\rm eff}\ (x)$ is the value of $R_{\rm eff}$ at $A_V^{\rm cl} = x$. However, the estimated uncertainty in the power-law exponent is comparable to the value of this exponent, so the positive slope seen in the $R_{\rm eff}$ versus $A_V^{\rm cl}$ curve is not statistically significant. Thus, we will instead interpret our result as an upper limit on the steepness of this curve, conservatively setting bounds of -0.06 and 0.50 on the value of the exponent by respectively subtracting and adding twice the uncertainty to the nominal value. We can then express corresponding limits on the overall steepness of the $R_{\rm eff}$ versus $A_V^{\rm cl}$ curve as $0.9 < R_{\rm eff}(20\ {\rm mag})/R_{\rm eff}(2\ {\rm mag}) < 3.2$.

Given the lack of statistically significant changes in $R_{\rm eff}$, we next proceed to derive a best estimate for the characteristic mean value of $R_{\rm eff}$ for the $A_V^{\rm cl}$ range that we have studied, along with an estimated uncertainty in this $R_{\rm eff}$ value. We do this by fitting a Gaussian function to the distribution of $R_{\rm eff}$ values shown in Figure 10 (top), which includes all objects from the "extended" ideal stellar sample. In this histogram, higher weights are given to points proportional to the number of times each star was found inside the ideal stellar locus, considering all of the systematic variations discussed in Section 5.3. With that calculation, we find $R_{\rm eff} = 2.4 \pm 0.8$, where the uncertainty is here estimated to be equal to the 1σ width of the distribution.

Figure 10 (bottom) shows a direct comparison between p_{500} and p_I/τ_V using the same "extended" ideal stellar sample. The red and green lines in that diagram represent the mean $R_{\rm eff}$ value as well as its uncertainty, respectively, as determined from the Gaussian fit in Figure 10 (top). Since the $R_{\rm eff}$ versus $A_V^{\rm cl}$ curve is not perfectly flat (Figure 9, top right), the distribution of points in the p_{500} versus p_I/τ_V diagram is not expected to exactly match the slope of the red line, which assumes a direct proportionality between the two quantities. Computing the correlation coefficient between p_{500} and p_I/τ_V for each variation of the GL method, and taking the average value, we obtain $\langle R^2 \rangle = 0.63$, demonstrating that a significant correlation exists between these quantities.

6. Discussion

6.1. Polarization Properties in the $2 < A_V < 20$ mag Range

The main goal of this work was to compute the polarization efficiency ratio, $R_{\rm eff}$. In addition to $R_{\rm eff}$, in Section 5.3, we investigated how p_{500} and p_I/τ_V vary as a function of $A_V^{\rm cl}$, in order to understand how these two quantities separately affect $R_{\rm eff}$. We found that, in the range $2\ {\rm mag} < A_V^{\rm cl} < 20\ {\rm mag}$, both p_{500} and p_I/τ_V show decreasing trends, with power-law exponents of -0.26 ± 0.07 and -0.47 ± 0.17, respectively (see Figure 9, right panels).

Fissel et al. (2016) presented a detailed analysis of the BLASTPol data set for Vela C, including studies of p_{500} as a function of $A_V^{\rm cl}$. These authors found a decreasing trend, corresponding to a power-law exponent of -0.45. The apparent discrepancy between this value and our -0.26 exponent probably arises from the fact that Fissel et al. (2016) studied the entire range of cloud depths between $A_V^{\rm cl} \sim 2$ mag and $\sim$50 mag, whereas in this work we only used the subset of BLASTPol data for which correlation with ideal stars was possible. This subset covers $2\ {\rm mag} < A_V^{\rm cl} < 20\ {\rm mag}$. It is clear from Figure 12 of Fissel et al. (2016) that for low column density sight lines, the p_{500} versus $A_V^{\rm cl}$ curve is relatively flatter than what is seen deeper in the cloud, consistent with our observation of a shallower exponent for our lower-density sight lines.

The power-law exponents we found for both the submillimeter (-0.26) and near-IR (-0.47) data are comparable to what has been found in similar studies that have been carried out for other molecular clouds (Gerakines et al. 1995; Goodman et al. 1995; Matthews et al. 2002; Whittet et al. 2008; Chapman et al. 2011; Cashman & Clemens 2014; Alves et al. 2014; Jones et al. 2015). These studies used either near-IR or submillimeter data, or sometimes a combination of the two, and found exponents generally lying in the range -0.3 to -1.0. Jones et al. (2015) show that for the largest column densities the exponents tend to be more negative, consistent with our qualitative observations concerning Figure 12 of Fissel et al. (2016).

The well-known tendency for $p_{\rm em}$ and $p_{\rm ex}/\tau_V$ to decrease with column density has been modeled in several papers. For example, it has been interpreted as an effect of turbulence (Falceta-Gonçalves et al. 2008), as a loss of grain alignment toward well-shielded regions (Whittet et al. 2008), or as a combination of both effects (Jones et al. 2015).

In Section 5.4, we showed that $R_{\rm eff}$ shows no statistically significant changes with $A_V^{\rm cl}$ over the sampled range of $2\ {\rm mag} < A_V^{\rm cl} < 20\ {\rm mag}$. As previously discussed, if we assume that the same population of dust grains distributed along the LOS is producing both polarized emission and polarization by extinction, $R_{\rm eff}$ should depend only on intrinsic grain properties. In quiescent molecular clouds, grain processing effects, such as growth due to coagulation, may take place as one goes deeper into the cloud (Draine 2003; Jones 2004). Potentially, these could affect $R_{\rm eff}$. The relatively flat profile of $R_{\rm eff}$ versus $A_V^{\rm cl}$ that we have found for Vela C implies that any changes in $R_{\rm eff}$ that are occurring in the cloud due to changes in dust grain properties with increasing $A_V^{\rm cl}$ must be too small for us to detect given our sensitivity limitations. From the discussion in Section 5.4, we conclude that no change in $R_{\rm eff}$ larger than about a factor of three is occurring over the $A_V^{\rm cl}$ range sampled. We cannot rule out the possibility that much larger changes in $R_{\rm eff}$ occur for $A_V^{\rm cl} > 20$ mag.

6.2. Observations and Predictions of $R_{\rm eff}$ for the Diffuse ISM

Our value of 2.4 ± 0.8 for $p_{500}/(p_I/\tau_V)$ can in principle be compared against the prediction of dust grain models that are able to link the polarization extinction and emission spectra. Draine & Fraisse (2009) present four such models, in which observed polarization spectra at optical/near-IR wavelengths are used as inputs (Serkowski et al. 1975; Martin et al. 1992). One of the output products of the model is the polarized emission spectrum, allowing a direct comparison of $p_{\rm em}$ with $p_{\rm ex}/\tau_V$ for specific wavelengths. However, these models were designed to reproduce the conditions of the diffuse atomic ISM,

so a direct comparison with our results is problematic. The *Planck* collaboration carried out a comparison between polarized emission at 850 μm and published V-band starlight polarization for diffuse emission sight lines (Planck Collaboration Int. XXI 2015). A polarization efficiency ratio of $p_{850}/(p_V/\tau_V) = 4.2 \pm 0.3$ was obtained, which may be compared with the predictions by Draine & Fraisse (2009) of $2.9 - 4.1$ for the same quantity.

Planck Collaboration Int. XXI (2015) also determined P_{850}/p_V (where P_{850} is the polarized *flux* at 850 μm), which also may be compared against models. As pointed out by Planck Collaboration Int. XXI (2015), this quantity is easier to measure since it is independent of the typical systematic uncertainties that affect τ_V. In the case of molecular clouds, however, the emission depends on grain temperature (which usually decreases for higher densities; Fissel et al. 2016), so P_{500}/p_I is also expected to vary. Therefore, in this work we focused only on $p_{500}/(p_I/\tau_V)$.

Despite the above-mentioned mismatch between our observations and the model of Draine & Fraisse (2009), we will compare our value for $p_{500}/(p_I/\tau_V)$, which is 2.4 ± 0.8, to the Draine & Fraisse (2009) predictions, which are $\sim$3.3 for diffuse ISM models in which both carbonaceous and silicate grains are aligned, and $\sim$4.6 when only alignment by silicate grains is considered. This range of values was obtained by combining Figures 8 and 6 from Draine & Fraisse (2009). Of course we cannot draw scientific conclusions from this comparison, but we will note that the spread in the model $R_{\rm eff}$ values is comparable to the uncertainty in our observed value of $R_{\rm eff}$. Thus, if corresponding models for molecular cloud dust grains become available, and if there is a similar spread in $R_{\rm eff}$ values among the models, then with modest reduction in the observational uncertainties it will become possible to discriminate among the models using observed $R_{\rm eff}$ values.

6.3. Diffuse ISM Far-background Contamination in the Determination of $R_{\rm eff}$

The "standard analysis" of polarization properties (described in Section 5.3) was applied to strips 0–5. As before, each variation of the GL method (see Appendix D) leads to different power-law fits of $R_{\rm eff}$ versus $A_V^{\rm cl}$, p_{500} versus $A_V^{\rm cl}$, and p_I/τ_V versus $A_V^{\rm cl}$. Just as for the ideal strip, by taking the average of the power-law exponents, an "average curve" is obtained for each strip. Figure 11 shows the results of this analysis, in which all curves correspond only to the average curve obtained for each strip (different colors and line styles are associated with different strips, according to the label at the top). The red curves are the same as displayed in Figure 9 (right), corresponding to the ideal strip.

Figure 11 (top) shows that the inclusion of stars contaminated by the background material significantly affects the analysis of $R_{\rm eff}$. It is obvious that for strips 2–5, for which stars are increasingly contaminated by the far-background ISM, the $R_{\rm eff}$ versus $A_V^{\rm cl}$ curves are all displaced toward higher values in comparison with the curve from the ideal strip (red curve). This is especially true for lower cloud extinctions. Strips 0 and 1 were defined to be below and above the ideal strip (see Figure 8), respectively, but also share a subset of stars located in this strip. Therefore, they appear to suffer mildly from the displacement effect (they can be regarded as lower and upper

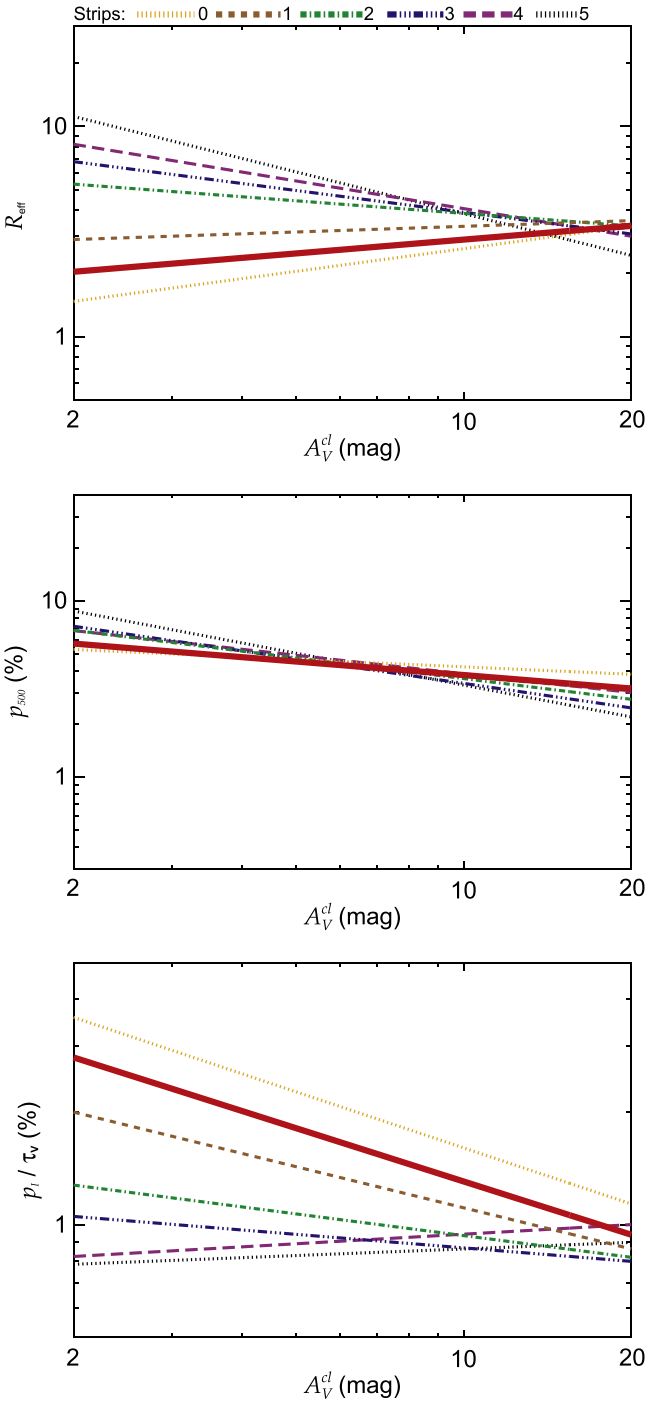

Figure 11. Average curves of polarization parameters as a function of cloud extinction $A_V^{\rm cl}$ for objects located within strips 0–5 (see Figure 8). Top left, top right, and bottom panels show curves for the polarization efficiency ratio $R_{\rm eff} = p_{500}/(p_I/\tau_V)$, p_{500}, and p_I/τ_V, respectively. The average curves in each case are obtained after applying the "standard analysis" described in Section 5.3 and in Appendix D. The average curves for the ideal stellar locus (red) are shown for reference and are identical to the ones shown in Figure 9 (right).

limits to the ideal strip curve), and, similar to the ideal strip curve, they also exhibit a slowly increasing trend with $A_V^{\rm cl}$.

When the curves for p_{500} and p_I/τ_V are analyzed separately (Figure 11, respectively middle and bottom), it becomes obvious which of these two parameters are most affected by the background contamination. The submillimeter polarized emission alone should not depend on the degree to which stars

are contaminated by the background material. As expected, all p_{500} versus $A_V^{\rm cl}$ curves overlap, with only slight variations. For p_I/τ_V versus $A_V^{\rm cl}$, however, the curves corresponding to the various strips show very significant differences in behavior. On the one hand, strips closer to the cloud (0, 1, and ideal) show the characteristic decrease with $A_V^{\rm cl}$. On the other hand, objects increasingly affected by the far-background ISM (represented by strips 2–5) show lower p_I/τ_V values and profiles more consistent with a flat trend, as a function of $A_V^{\rm cl}$. If the radiation from far-background sources is being affected by extra layers of interstellar material behind the cloud, then while the column density (and therefore τ_V) is expected to be higher, p_I should not necessarily increase in direct proportion, because different layers could have different magnetic field orientations. This scenario is consistent with the lower p_I/τ_V values observed in strips 2–5.

It is interesting to notice, however, that even considering the background contamination for strips 2–5, in Figure 11 (top), all $R_{\rm eff}$ versus $A_V^{\rm cl}$ curves seem to converge at the highest cloud extinctions probed by our sample. This suggests that at increasingly higher cloud extinctions, because the relative amount of cloud material along the LOS is large compared to the background diffuse ISM, the presence of background contamination becomes negligible for the purposes of calculating the polarization efficiency ratio. In addition, this shows that for higher extinctions, even if clumping and beam-averaging effects become important (see Appendix A), this does not affect the calculation of $R_{\rm eff}$ in a significant way. The convergence at $R_{\rm eff}$ values close to 2.4 for all curves at higher extinctions provides extra confidence that the application of the GL method was successful in determining the ideal subset of stars used for this work.

7. Conclusions

We have carried out the first large-scale quantitative comparison of near-IR and submillimeter polarization magnitudes measured toward the same molecular cloud. Our aim was to study the polarization efficiency ratio, which provides a constraint for physical grain models. For the Vela C molecular cloud, we combined polarized emission data from BLASTPol at 500 μm with starlight polarimetry in the I band. We also used complementary data from 2MASS, *Herschel*, and *Planck*. The main conclusions are summarized below.

1. The average polarization efficiency ratio ($R_{\rm eff} = p_{500}/(p_I/\tau_V)$) is found to be 2.4 ± 0.8 for cloud visual extinctions between $\sim$2 mag and $\sim$20 mag. This value can be used to test dust grain models designed specifically for the environment found inside molecular clouds.
2. We have examined the dependence of $R_{\rm eff}$ on cloud visual extinction, and we find no statistically significant deviations from a flat trend over the range of extinctions probed.
3. The polarization efficiency ratio is shown to vary significantly if far-background objects (contaminated by the diffuse background ISM) are included. This effect highlights the importance of selecting suitable stellar objects, such that the columns of material probed by polarized extinction and emission are similar. Nevertheless, we find that at higher cloud extinctions, the effect of the background contamination is negligible, since the relative contribution from the molecular cloud itself is dominant.

The type of study conducted here would significantly benefit from more precise distance determinations. Complementary data sets that could improve the near-IR versus submillimeter polarimetric comparison include products from trigonometric distance surveys such as the next *GAIA* data releases. In addition, as previously mentioned, dust grain models specifically developed for molecular clouds are needed for a meaningful comparison. Grain models that are suitable for predicting $R_{\rm eff}$ in this environment have yet to be developed and would be valuable tools for understanding which particular changes in grain properties are taking place in molecular clouds, thereby affecting the polarization efficiency ratio.

We are grateful to the anonymous referee for the valuable suggestions and comments. The BLASTPol collaboration acknowledges support from NASA (through grant numbers NAG5-12785, NAG5-13301, NNGO-6GI11G, NNX0-9AB98G, and the Illinois Space Grant Consortium), the Canadian Space Agency (CSA), the Leverhulme Trust through the Research Project Grant F/00 407/BN, Canada's Natural Sciences and Engineering Research Council (NSERC), the Canada Foundation for Innovation, the Ontario Innovation Trust, and the US National Science Foundation Office of Polar Programs. C. B. Netterfield also acknowledges support from the Canadian Institute for Advanced Research. F.P.S. was supported by the CAPES grant 2397/13-7. We thank the Columbia Scientific Balloon Facility (CSBF) staff for their outstanding work. F.P. thanks the European Commission under the Marie Sklodowska-Curie Actions within the H2020 program, Grant Agreement number: 658499—PolAME—H2020-MSCA-IF-2014. We thank the staff of OPD/LNA (Brazil) for their invaluable help during our observing runs. This investigation made extensive use of data products from the Two Micron All Sky Survey (2MASS), which is a joint project of the University of Massachusetts and the Infrared Processing and Analysis Center/California Institute of Technology, funded by the National Aeronautics and Space Administration and the National Science Foundation. We are grateful to Drs. A. M. Magalhães and A. Pereyra for providing the polarimeter and software used for the near-IR data reduction.

Facilities: BLASTPol, LNA: 1.6 m, LNA: 0.6 m.

Appendix A
Factors Affecting the Stellar Extinction ($A_V^{\rm st}$) Distributions

Below we list three factors that may explain the relatively wide distribution of $A_V^{\rm st}$ values observed toward regions having fixed cloud extinction $A_V^{\rm cl}$, when considering nonforeground stars in the wide photometric field data set (e.g., Figures 6, 7, and 15). Our aim is to identify which factor is dominant.

1. Photometric errors or uncertainties associated with assumptions used in the $A_V^{\rm st}$ calculation method (Section 4.2): The statistical uncertainties $\sigma A_V^{\rm st}$ derived solely through propagation of errors (from 2MASS J, H, and K_s magnitudes) typically range between 0.3 and 0.8 mag. These correspond to lower limits for the true uncertainties, which may also be affected by systematic effects such as variations in grain properties (which influence the total-to-selective extinction ratio and consequently the conversion between $E(J-K_s)$ and $A_V^{\rm st}$, as discussed in Section 4.2) and uncertainties in intrinsic colors. The combined statistical and systematic

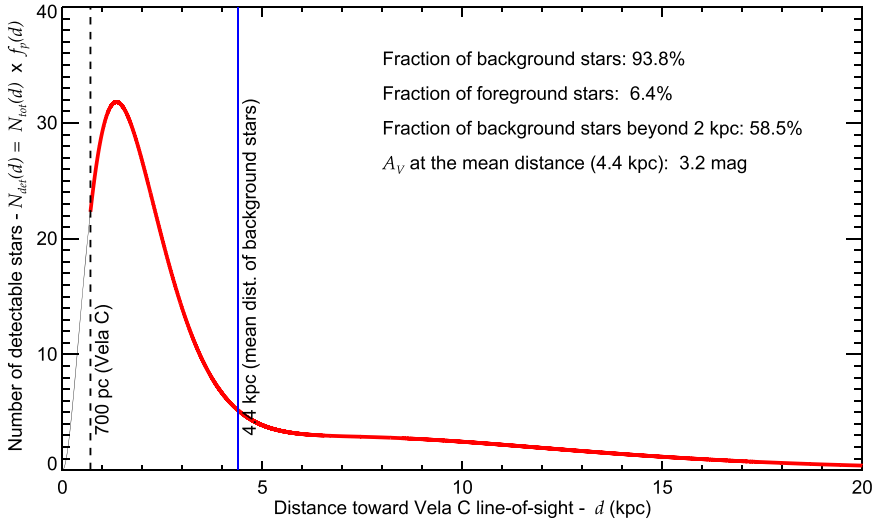

Figure 12. Number of detectable 2MASS stars ($N_{\rm det}$) as a function of distance d toward Vela C, according to estimates from Galactic stellar distribution models combined with the estimated photometric sensitivity of 2MASS. Extinction information used to obtain this curve is derived from the Galactic extinction model of Amôres & Lépine (2005) in combination with results from *Planck* (see discussion in Appendix A).

uncertainties in $A_V^{\rm st}$ are $\sim$1.5 mag, as discussed in Section 5.2 and in Appendix D.

2. Stars distributed over a range of distances and thus possibly contaminated by far-background material: It is possible to estimate statistically the fraction of stars in our wide photometric field sample that are located respectively in the foreground and background, by combining a simple model of the Galactic stellar distribution with information regarding the 2MASS sensitivity for our sample. A standard stellar distribution model (Bahcall 1986) gives the total number density of stars n_{tot} as a function of the Galactic radius r and perpendicular distance from the Galactic plane z:

$$n_{\rm tot}(r, z) = n(R_0) e^{-z/z_0} e^{-(r-R_0)/h}, \quad (4)$$

where R_0 is the distance from the Sun to the Galactic center ($\approx$8 kpc), $n(R_0)$ is the number density of stars in the solar neighborhood ($\approx$0.13 stars/pc^3), z_0 is the scale height ($\approx$250 pc), and h is the disk scale length ($\approx$3.5 kpc). This equation can be rewritten in terms of d, defined as the distance from the Sun along the Vela C LOS, using $r^2 = R_0^2 + d^2 - 2dR_0\cos(l)$ and $z = d\sin(b)$ (where l and b are the cloud's Galactic longitude and latitude, respectively taken as 266° and 1°). The total number of stars in a field of view of area $A(d)$ may be found by integrating the function $N_{\rm tot}(d) = A(d) n_{\rm tot}(d)$ along d. Finally, the actual number of stars detected by 2MASS is given by $N_{\rm det}(d) = f_p(d) N_{\rm tot}(d)$, where $f_p(d)$ is the total fraction of stars that are detectable given the 2MASS sensitivity, as a function of distance d (see below).

Using standard methods (e.g., Santos et al. 2012), we find that for the wide photometric field the photometric completeness limits are given by ($J_{\rm cl}$, $H_{\rm cl}$, $Ks_{\rm cl}$) = (15.3, 14.5, 14.3). The J and H values are slightly smaller than the canonical 2MASS limits (given by 15.8 and 15.1, respectively; Skrutskie et al. 2006), because our sample selects only stars with "AAA" 2MASS photometric quality and excludes points outside the reddening band (see Section 4.2). With these completeness limits (referred to as $m_{\rm cl}$), the maximum distance $d_{\rm max}$ at which a star of a given spectral type and luminosity class can be detected may be obtained through $m_{\rm cl} - M_\lambda = 5\log(d_{\rm max}) - 5 + A_\lambda$, where M_λ is the intrinsic magnitude (Koornneef 1983; Carpenter 2001; Wegner 2007) and A_λ is the extinction at each band (converted to A_V using canonical relations; Fitzpatrick 1999). Combining $d_{\rm max}$ with the information on the typical fractions for each stellar type (e.g., Ledrew 2001), we find that the fraction function for our sample is approximately given by $f_p(d) = e^{-0.0014d} + 0.0018$. To derive this curve, we also use models of Galactic extinction from Amôres & Lépine (2005) to estimate the extinctions of diffuse matter as a function of distance toward Vela C. The saturating extinction levels at high distances ($\approx$20 kpc) given by this model ($\approx$3.3 mag) do not agree with nearby off-cloud extinctions derived from *Planck* for the same Galactic latitudes ($\approx$6 mag). This difference might be due to increased submillimeter optical depth per unit column density near the Galactic plane (see Section 4.3) or diffuse molecular material not being accounted for in the Amôres & Lépine (2005) model. We scaled the extinction values from Amôres & Lépine (2005) by a factor of 1.8 so that the saturating A_V values at high distances correspond to the values found by *Planck*. Note that even without this scaling, the mean far-background $A_V^{\rm st}$ values found for the wide photometric field are still fairly large, as will be discussed below.

The function $N_{\rm det}(d)$ gives the total number of detectable stars as a function of distance, as shown in Figure 12. Giants and supergiants in general are bright enough to be detected at large distances (>10 kpc). The mean stellar distance of the background stars according to this model is $\sim$4.4 kpc, with a broad distribution peaking at $\sim$1.3 kpc. At this mean distance, the A_V according to the models is 3.2 mag. If the extinctions from Amôres & Lépine (2005) are not scaled to match *Planck* (as described above), then we find that the A_V at the mean stellar distance is $\approx$2.1 mag. The range of stellar extinctions 2.1–3.2 mag is consistent with the mean $A_V^{\rm st}$ for the wide photometric field off-cloud stars (black histogram in Figure 7, top left). Integrating the curve of Figure 12, we find that the fractions of expected foreground and background detected stars are

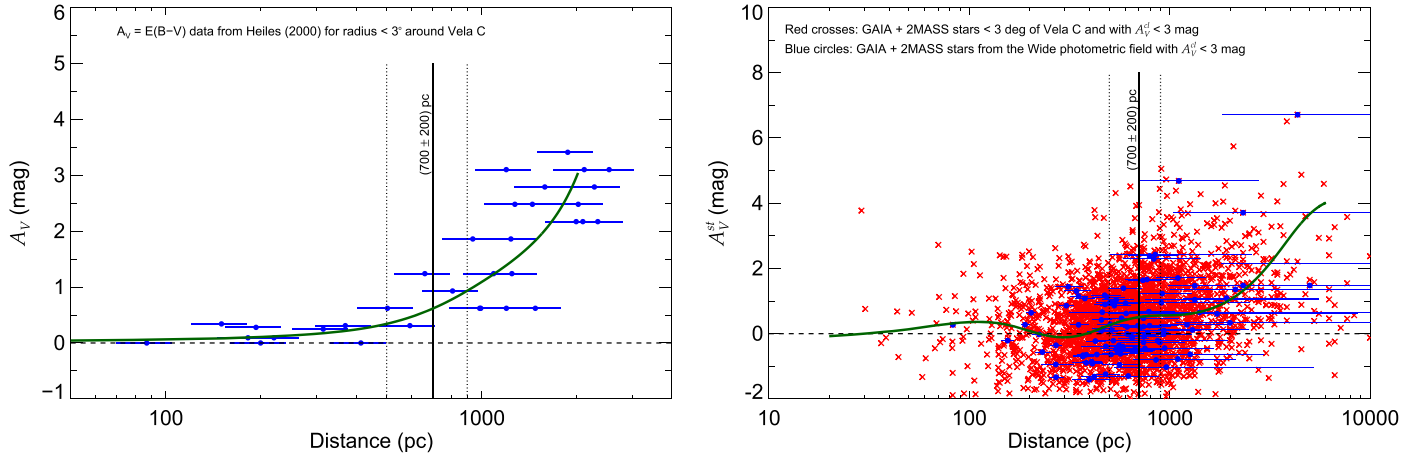

Figure 13. Left: visual extinction (A_V) as a function of distance within 3° of Vela C from Heiles (2000), probing the diffuse material around the cloud. The error bars in distance represent typical uncertainties of 20% (based on agreement between different catalogs, according to Heiles 2000). Right: stellar extinction A_V^{st} as a function of distance within 3° of Vela C for *GAIA* stars combined with 2MASS data (red crosses). Blue dots represent the fraction of this sample in the "wide photometric field" (see Table 1). Stars in the direction of the Vela C cloud itself ($A_V^{cl} > 3$ mag) were excluded. For clarity, error bars in distance are shown only for the blue dots. For both graphs, the solid green curve is a spline fit to the binned averaged data, to show the general trend.

respectively 6% and 94%. It is also worth pointing out that the fraction of background stars located beyond 2 kpc is ≈59%, showing that a significant fraction of the detected stellar sample is expected to be located in the far background. Thus, A_V^{st} is probably significantly affected by background material, which is shown to be nonnegligible in the general direction of Vela C (see Section 4.5 and Appendix B).

3. Beam averaging over cloud "holes" and clumps: The difference between the finite *Herschel* beam and the stellar pencil beam introduces an additional source of spread in the A_V^{st} values (see below).

In order to evaluate the relative importance of these three factors, consider Figure 7 (top left), which shows the distribution of A_V^{st} for objects surrounding the cloud ($0 < A_V^{cl}(\text{mag}) < 2$). The distribution FWHM is about 6 mag, which cannot be explained by A_V^{st} photometric uncertainties, as the ∼1.5 mag statistical errors in A_V^{st} lead to an FWHM of ≈3.5 mag. In addition, we find it unlikely that dense clumps would be found in this area, since it represents a more diffuse material around the cloud, and therefore beam averaging (see item 3 above) seems unlikely to play a major role. We conclude that the dominant factor controlling the spread of A_V^{st} values is the wide range of stellar distances. This conclusion is also supported by evidence presented in Section 4.5 and Appendix B. For higher A_V^{cl} values, even if clumping and beam averaging are more significant, these factors do not appear to affect the $R_{\rm eff}$ calculation (see Section 6.3).

Appendix B
Additional Evidence for the Existence of Far-background Interstellar Material

In addition to the *Planck* data presented in Section 4.5, additional evidence can be gathered from the literature supporting the existence of far-background diffuse interstellar material. First, from the Heiles (2000) compilation of polarimetric and photometric data, 33 stars are found within a radius of 3° around Vela C (centered on RCW 36). These objects are spatially located in diffuse lines of sight surrounding the cloud, so they serve as adequate probes of the diffuse material in the disk of the Galaxy as a function of distance. Figure 13 (left) shows a plot of A_V versus distance (pc), where A_V is derived from color excess data $E(B-V)$ (using the general relation $A_V = 3.1E(B-V)$). Visual extinctions increase as a function of distance, a trend that continues for distances greater than 1 kpc. The monotonic increase continues up to the maximum distance of this data set (≈2.5 kpc), reaching levels around 3 mag, which is consistent with the center of the broad A_V^{st} distribution in Figure 7 (top left).

Next, we combined trigonometric parallaxes from the *GAIA* early data release (Gaia Collaboration et al. 2016) with 2MASS, within a 3° radius around Vela C. Stellar extinctions were calculated according to the method described in Section 4.2. In this area, 2945 *GAIA* stars with valid parallax detections are found, after selecting only objects toward more diffuse lines of sight ($A_V^{cl} < 3$ mag). Among this total, 102 objects are part of the wide photometric field data set defined in Table 1. Figure 13 (right) shows a plot of A_V^{st} as a function of distance. Red crosses represent the 2945 objects within 3° of Vela C, while blue dots represent the fraction of these points corresponding to the wide photometric field. The stellar distribution (including wide photometric field objects) reaches very large distances in the far background, up to approximately 10 kpc, consistent with the discussion of Appendix A. The *GAIA*+2MASS combination shows a trend similar to the one found from the Heiles (2000) data: for distances smaller than the cloud's location (700 pc), the foreground stars show a distribution of stellar extinctions close to 0 mag, but a clear increase in A_V^{st} is found for higher distances. Notice that for large distances, the distribution reaches values as high as 6 mag for some objects. This reinforces the idea that a significant number of far-background stars contaminated by diffuse material behind the cloud are present within our sample.

Appendix C
Determination of the Foreground Levels of Extinction and Polarization

Franco (2012) investigated the extinction levels in the general direction of Vela and Puppis within the 0–1000 pc distance range, using *uvby*Hβ Strömgren photometry. Although some ISM features are found in this direction (such as the edge

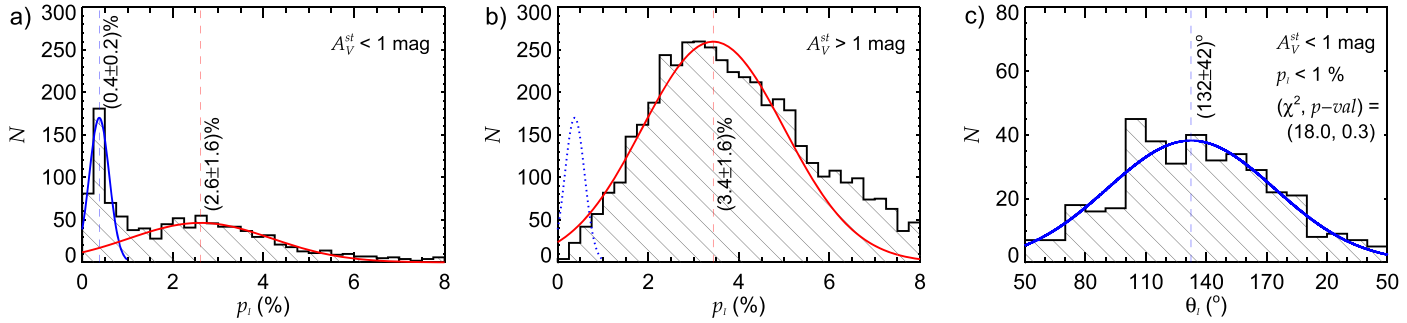

Figure 14. Analysis of the foreground polarization component using the *I*-band–2MASS combination data set (see Table 1): panels (a) and (b), respectively, show the distributions of polarization fraction in the *I* band for ranges of stellar extinctions defined by $A_V^{st} < 1$ mag and $A_V^{st} > 1$ mag. Solid red and blue curves are Gaussian fits to the sample. Panel (c) shows a histogram of equatorial polarization angles for objects with $A_V^{st} < 1$ mag and $p_I < 1\%$ (corresponding to the peak shown in blue in panel (a)). The chi-squared (and associated p value) is shown only for the Gaussian fit in panel (c) (in panel (a) the red Gaussian contaminates the chi-squared calculation for the blue Gaussian).

of the Local Bubble, the Gum Nebula, and the Vela Supernova Remnant), the overall color excess levels suggest that the material out to 700 pc is very diffuse and has very low density. In particular, areas labeled as SA173 and SA171 from Franco (2012) are located respectively above and below the Galactic plane, with an angular separation of a few degrees relative to the VMR. The median $E(b-y)$ values out to 700 pc for these areas are 0.05 and 0.03 mag, which correspond to $A_V = 0.22$ and 0.13 mag (assuming $A_V = 4.3E(b-y)$; Crawford & Mandwewala 1976), respectively. Similarly, Reis et al. (2011) used *uvby*Hβ photometry to map stellar distances and extinctions in the local ISM. For sky positions within 3° of Vela C, 17 stars distributed out to 500 pc were found from their sample, with a mean A_V of 0.10 mag. These estimates show that the foreground ISM in the direction of the VMR is typically very diffuse, consistent with "tunnels" observed in this direction from maps of the local ISM (Lallement et al. 2003; Welsh et al. 2010; Reis et al. 2011). Based on the above-mentioned foreground extinction values, we estimate an average foreground extinction level of approximately 0.15 ± 0.09 mag toward the Vela LOS.

In order to estimate the foreground polarization component, we first define a conservative upper limit for the foreground stellar extinction of ≈1 mag, based on the observation that in Figure 6 (top) most of the stars in the "band" that defines the foreground objects are below this limit. The results from this analysis remain essentially unaltered if this choice is varied within reasonable limits (see below). Subsequently, we analyze the distribution of p_I for objects from the *I*-band–2MASS combination data set (see Table 1) possessing stellar extinction values below this upper limit. This is shown in Figure 14(a). We compare this histogram with the one for $A_V^{st} > 1$ mag, shown in Figure 14(b). In the first histogram, we notice a peak centered on low polarization values, around ≈0.4% (blue Gaussian curve). This peaked distribution is obviously absent in the second histogram (for reference, it is shown as a dotted blue line). Instead, it shows a broad distribution centered on much higher polarization values (around 3.4%). This indicates that the stars within the peak shown in blue are mostly foreground objects. In addition to the analysis of color excess as a function of distance, Franco (2012) also studied linear polarization in the *B* band toward this general direction, showing that levels between 0 and 0.60% may be found out to 700 pc. This corresponds to a range of values between 0 and ≈0.54% in the *I* band, (assuming the general spectral relation by Serkowski et al. 1975), which is consistent with the distribution of values seen within the peak shown in blue in Figure 14(a).

In order to find the mean foreground polarization orientation, we use the histogram of position angles in Figure 14(c), which includes only stars with $A_V^{st} < 1$ mag and $p_I < 1\%$ (these criteria are used to select only the stars within the peak shown in blue in Figure 14(a)). We find a broad distribution of polarization angles peaked at $\theta_I = 132°$. Although a large spread is expected for such low polarization levels (the typical p_I S/N for this particular sample is just above the threshold of 3, so the angle uncertainties are ≈10°), this distribution suggests that the intervening diffuse ISM features located in the foreground might have a wide range of magnetic field orientations. However, the peak of the distribution is a reasonable estimate since it represents the most common orientation found in this distance range. We therefore adopt $p_I = 0.4\%$ and $\theta_I = 132°$ as the foreground polarization fraction and angle toward Vela C.

These results are robust with respect to the choice of the A_V^{st} upper limit. If instead of 1 mag, levels of 0.5 or 2 mag are chosen, the estimated p_I and θ_I from the foreground remain fixed, although the spreads in the Gaussian distributions from which they are derived vary slightly.

Appendix D
Detailed Description of the Gaussian-logistic Method and Its Sources of Systematic Uncertainties

As described in Section 5.2, the first term of Equation (2) corresponds to the foreground stellar population, previously identified as the "band" of points roughly parallel to the $A_V^{st} = 0$ line in Figure 8. For a given A_V^{cl} bin, the parameters α, β, and σ (the height, displacement, and width, respectively) define a Gaussian curve. The displacement and width of the Gaussian distribution should be independent of A_V^{cl}, since the extinction of foreground objects is not affected by the cloud. Therefore, the first step before applying GL fits is to obtain single values of β and σ to be used for all A_V^{cl} bins. We define a population of foreground objects in Figure 8 as the objects inside the gray box (delimited by $A_V^{cl} > 6$ mag and $A_V^{st} < 3.5$ mag), and we show the A_V^{st} distribution for the corresponding stars as the first histogram in Figure 15 (top left). A simple Gaussian fit to this distribution gives $\beta = -0.1$ mag and $\sigma = 1.5$ mag. For each A_V^{cl} bin, the number of foreground stars obviously changes significantly, and therefore the only Gaussian parameter allowed to vary in the

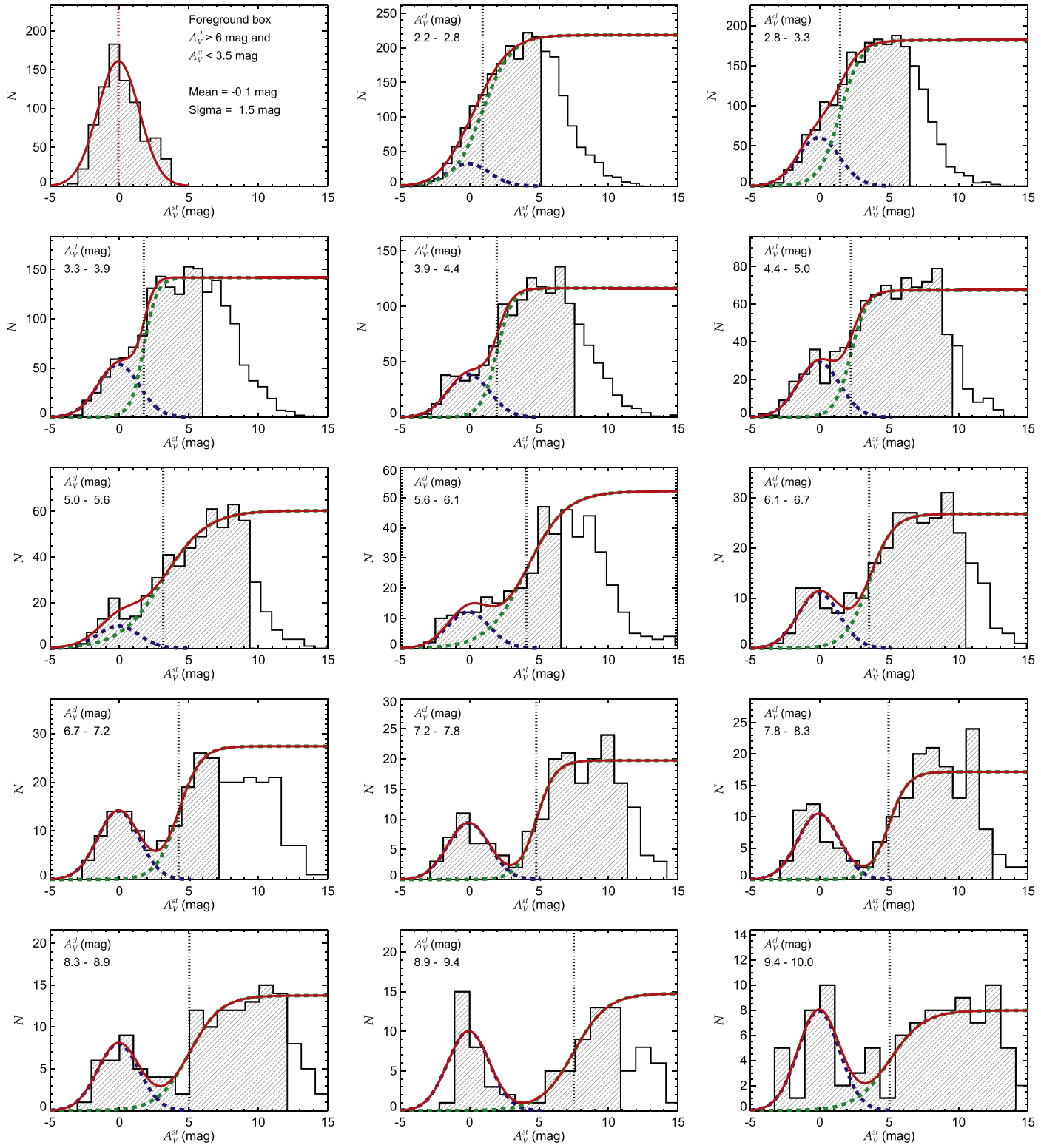

Figure 15. Distributions of stellar extinctions ($A_V^{\rm st}$) for different cloud extinction ($A_V^{\rm cl}$) bins, using objects from the wide photometric field (see Table 1), illustrating the GL procedure. The first histogram at the top left represents the distribution of foreground stars located inside the gray box defined in Figure 8, from which the Gaussian parameters β and σ are obtained and used as inputs for the GL fits. All other distributions are defined within narrow $A_V^{\rm cl}$ bins and used to fit the GL function (the red curve, with the Gaussian and logistic components separately defined by the blue and green curves). The shaded areas of each histogram represent the points effectively used in the fits (the drop in the number of stars at higher extinctions is ignored). The vertical dotted black lines are the midpoints of the logistic functions fit in each case, used to define the position of the yellow circles in Figure 8. For this particular run of the GL method, we use $N_{\rm d} = 18$, $R_{\rm bin} = 5$ mag, and $N_{\rm max} = 1$, which correspond to the standard example (see description in the text).

following analysis is α (the height of the Gaussian curve). It is interesting to note that the 1.5 mag spread in the foreground stellar extinction provides a good estimate of the total uncertainty in A_V^{st} (which includes both statistical and systematic errors; see Section 5.1).

The next step is to build histograms of A_V^{st} for different A_V^{cl} bins; one can imagine dividing the diagram in Figure 8 into a series of vertical bands with fixed ΔA_V^{cl} widths, and an A_V^{st} histogram is drawn for each of these vertical bands. For $A_V^{cl} > 10$ mag the number of points is usually insufficient to apply GL fits, so the GL method is not applied to these points. The histograms are shown in Figure 15 (all panels except for the first one). As A_V^{cl} increases, it is easy to distinguish the foreground (Gaussian-like) population at low extinction, followed by a "gap," and finally a steep rise defining the ideal stars, as previously depicted in the schematic of Figure 4. The GL function (Equation (2), shown by the red curves) is then fit to each of these distributions; as described above, while β and σ are held constant, parameters α (the height of the Gaussian function), a (the height of the logistic function), b (the steepness of the curve), and A_V^0 (the midpoint of the logistic function) are allowed to vary independently for each distribution. For cloud extinctions between $A_V^{cl} = 0$ and 2.2 mag, the distributions lead to bad fits and therefore are not shown. For such low A_V^{cl}, the foreground and ideal star populations are merged. The quantity A_V^0 is shown as a vertical dotted line in each histogram of Figure 15.

As mentioned in Section 5.3, the results from the GL method depend on certain choices of parameters because these affect the selection of ideal stars. The goal here is to identify the sources of systematics and vary them within reasonable values, repeating the entire GL analysis in each case. There are three parameters that can significantly affect the fits of the GL function to the histograms of Figure 15:

1. The number of A_V^{st} distributions (N_d) between $A_V^{cl} = 0$ and 10 mag, which naturally affects the A_V^{cl} bin widths for each histogram of Figure 15. For larger N_d, the number of points available for the GL fits inside each histogram decreases. For the particular case shown in Figure 8, we chose $N_d = 18$ (and therefore $\Delta A_V^{cl} \approx 0.56$ mag for each distribution). To account for systematics, values of $N_d = 18$, 14, and 10 were used.
2. The bin sizes ΔA_V^{st} for each distribution, which are defined according to the following relation: $\Delta A_V^{st} = R_{bin}/(\log N_{hist})$, where N_{hist} is the total number of elements in a given histogram and R_{bin} is a proportionality factor that may be varied. This allows the bin sizes to decrease or increase if the number of elements is, respectively, higher or lower. In Figure 8, we used $R_{bin} = 5$ mag. Here, values of $R_{bin} = 3$, 5, and 7 mag are used.
3. The maximum A_V^{st} to truncate the distributions in order to apply the GL fits. In each histogram of Figure 15, only the shaded area is used in the GL fits, because the drop in the number of stars for higher A_V^{st} is not accounted for in Equation (2) (the precise position where this drop occurs is not important for our purposes). Therefore, a maximum A_V^{st} needs to be chosen. In Figure 8, we set this maximum limit to be the position of the first bin after the highest peak of the histogram ($N_{max} = 1$). Here, values of $N_{max} = 0$, 1, and 2 are used.

As described above, the analysis shown in Figures 8, 9 (left), and 15 corresponds to the "standard example," in which we used the intermediate diffuse emission subtraction method along with $N_d = 18$, $R_{bin} = 5$ mag, and $N_{max} = 1$. Variations of these three quantities (allowing 27 different combinations) result in slight changes in the determinations of A_V^0 for each histogram. When considered as a whole, these variations also change the linear fit shown in Figure 8, which therefore affects the determination of the ideal stellar locus. In addition, the entire process is repeated separately using BLASTPol data sets with aggressive, conservative, and intermediate diffuse emission subtraction, leading to the results given in Figure 9 (right).

Another parameter that should be mentioned is the width chosen for the strips of Figure 8. We set the width of the strips to 1.5 mag, based on the estimated A_V^{st} uncertainties. Varying this width effectively increases or reduces the number of points inside each strip. We verified that such variation causes only minor changes in our final results. Because these changes are smaller than those caused by varying the three parameters discussed above, changes in strip width are not included in the formal systematic error analysis described here.

References

Alves, F. O., Frau, P., Girart, J. M., et al. 2014, A&A, 569, L1
Amôres, E. B., & Lépine, J. R. D. 2005, AJ, 130, 659
Andersson, B.-G., Lazarian, A., & Vaillancourt, J. E. 2015, ARA&A, 53, 501
Andersson, B.-G., Pintado, O., Potter, S. B., Straižys, V., & Charcos-Llorens, M. 2011, A&A, 534, A19
André, P., Men'shchikov, A., Bontemps, S., et al. 2010, A&A, 518, L102
Arzoumanian, D., André, P., Didelon, P., et al. 2011, A&A, 529, L6
Baba, D., Nagata, T., Nagayama, T., et al. 2004, ApJ, 614, 818
Bahcall, J. N. 1986, ARA&A, 24, 577
Bethell, T. J., Chepurnov, A., Lazarian, A., & Kim, J. 2007, ApJ, 663, 1055
Bohlin, R. C., Savage, B. D., & Drake, J. F. 1978, ApJ, 224, 132
Carpenter, J. M. 2001, AJ, 121, 2851
Cashman, L. R., & Clemens, D. P. 2014, ApJ, 793, 126
Chapman, N. L., Goldsmith, P. F., Pineda, J. L., et al. 2011, ApJ, 741, 21
Chiar, J. E., Adamson, A. J., Whittet, D. C. B., et al. 2006, ApJ, 651, 268
Clemens, D. P., & Tapia, S. 1990, PASP, 102, 179
Crawford, D. L., & Mandwewala, N. 1976, PASP, 88, 917
Davis, L., Jr., & Greenstein, J. L. 1951, ApJ, 114, 206
Dolginov, A. Z., & Mitrofanov, I. G. 1976, Ap&SS, 43, 291
Draine, B. T. 2003, ARA&A, 41, 241
Draine, B. T., & Fraisse, A. A. 2009, ApJ, 696, 1
Draine, B. T., & Weingartner, J. C. 1996, ApJ, 470, 551
Draine, B. T., & Weingartner, J. C. 1997, ApJ, 480, 633
Falceta-Gonçalves, D., Lazarian, A., & Kowal, G. 2008, ApJ, 679, 537
Fissel, L. M., Ade, P. A. R., Angilè, F. E., et al. 2016, ApJ, 824, 134
Fitzpatrick, E. L. 1999, PASP, 111, 63
Franco, G. A. P. 2012, A&A, 543, A39
Gaia Collaboration, Brown, A. G. A., Vallenari, A., et al. 2016, A&A, 595, A2
Gandilo, N. N., Ade, P. A. R., Angilè, F. E., et al. 2016, ApJ, 824, 84
Gerakines, P. A., Whittet, D. C. B., & Lazarian, A. 1995, ApJL, 455, L171
Goldsmith, P. F., Heyer, M., Narayanan, G., et al. 2008, ApJ, 680, 428
Goodman, A. A., Jones, T. J., Lada, E. A., & Myers, P. C. 1995, ApJ, 448, 748
Hall, J. S. 1949, Sci, 109, 166
Heiles, C. 2000, AJ, 119, 923
Hildebrand, R. H. 1983, QJRAS, 24, 267
Hildebrand, R. H. 1988, QJRAS, 29, 327
Hill, T., Motte, F., Didelon, P., et al. 2011, A&A, 533, A94
Hiltner, W. A. 1949, Sci, 109, 165
Hoang, T., Lazarian, A., & Martin, P. G. 2014, ApJ, 790, 6
Hsu, J.-C., & Breger, M. 1982, ApJ, 262, 732
Jones, A. P. 2004, in ASP Conf. Ser. 309, Astrophysics of Dust, ed. A. N. Witt, G. C. Clayton, & B. T. Draine (San Francisco, CA: ASP), 347
Jones, T. J. 1989, ApJ, 346, 728
Jones, T. J. 2015, in Magnetic Fields in Diffuse Media, Astrophysics and Space Science Library, Vol. 407, ed. A. Lazarian, E. M. de Gouveia Dal Pino, & C. Melioli (Berlin: Springer), 153

Jones, T. J., Bagley, M., Krejny, M., Andersson, B.-G., & Bastien, P. 2015, AJ, 149, 31
Kim, S.-H., & Martin, P. G. 1994, ApJ, 431, 783
Kim, S.-H., & Martin, P. G. 1995, ApJ, 444, 293
Koornneef, J. 1983, A&A, 128, 84
Lallement, R., Welsh, B. Y., Vergely, J. L., Crifo, F., & Sfeir, D. 2003, A&A, 411, 447
Larson, K. A., Whittet, D. C. B., & Hough, J. H. 1996, ApJ, 472, 755
Lazarian, A. 2007, JQSRT, 106, 225
Lazarian, A., & Draine, B. T. 2000, ApJL, 536, L15
Ledrew, G. 2001, JRASC, 95, 32
Liseau, R., Lorenzetti, D., Nisini, B., Spinoglio, L., & Moneti, A. 1992, A&A, 265, 577
Magalhaes, A. M., Rodrigues, C. V., Margoniner, V. E., Pereyra, A., & Heathcote, S. 1996, in ASP Conf. Ser. 97, Polarimetry of the Interstellar Medium, ed. W. G. Roberge & D. C. B. Whittet (San Francisco, CA: ASP), 118
Martin, P. G. 2007, in in EAS Publications Ser. 23, Sky Polarisation at Far-infrared to Radio Wavelengths: The Galactic Screen before the Cosmic Microwave Background, ed. M.-A. Miville-Deschenes & F. Boulanger (Cambridge: Cambridge Univ. Press), 165
Martin, P. G., Adamson, A. J., Whittet, D. C. B., et al. 1992, ApJ, 392, 691
Martin, P. G., Roy, A., Bontemps, S., et al. 2012, ApJ, 751, 28
Mathewson, D. S., & Ford, V. L. 1970, MmRAS, 74, 139
Matthews, B. C., Fiege, J. D., & Moriarty-Schieven, G. 2002, ApJ, 569, 304
McKee, C. F., & Ostriker, E. C. 2007, ARA&A, 45, 565
Moncelsi, L., Ade, P. A. R., Angilè, F. E., et al. 2014, MNRAS, 437, 2772
Mouschovias, T. C., & Paleologou, E. V. 1981, ApJ, 246, 48
Murphy, D. C., & May, J. 1991, A&A, 247, 202
Netterfield, C. B., Ade, P. A. R., Bock, J. J., et al. 2009, ApJ, 707, 1824
Pereyra, A. 2000, PhD thesis, Univ. São Paulo
Planck Collaboration XXV 2011, A&A, 536, A25
Planck Collaboration XI 2014, A&A, 571, A11
Planck Collaboration Int. XXI 2015, A&A, 576, A106
Rachford, B. L., Snow, T. P., Destree, J. D., et al. 2009, ApJS, 180, 125
Reis, W., Corradi, W., de Avillez, M. A., & Santos, F. P. 2011, ApJ, 734, 8
Rieke, G. H., & Lebofsky, M. J. 1985, ApJ, 288, 618
Santos, F. P., Franco, G. A. P., Roman-Lopes, A., Reis, W., & Román-Zúñiga, C. G. 2014, ApJ, 783, 1
Santos, F. P., Roman-Lopes, A., & Franco, G. A. P. 2012, ApJ, 751, 138
Savage, B. D., Bohlin, R. C., Drake, J. F., & Budich, W. 1977, ApJ, 216, 291
Serkowski, K., Mathewson, D. L., & Ford, V. L. 1975, ApJ, 196, 261
Skrutskie, M. F., Cutri, R. M., Stiening, R., et al. 2006, AJ, 131, 1163
Smith, C. H., Wright, C. M., Aitken, D. K., Roche, P. F., & Hough, J. H. 2000, MNRAS, 312, 327
Tody, D. 1986, Proc. SPIE, 627, 733
Turnshek, D. A., Bohlin, R. C., Williamson, R. L., et al. 1990, AJ, 99, 1243
Vaillancourt, J. E., & Andersson, B.-G. 2015, ApJL, 812, L7
Wardle, J. F. C., & Kronberg, P. P. 1974, ApJ, 194, 249
Wegner, W. 2007, MNRAS, 374, 1549
Welsh, B. Y., Lallement, R., Vergely, J.-L., & Raimond, S. 2010, A&A, 510, A54
Whittet, D. C. B., Hough, J. H., Lazarian, A., & Hoang, T. 2008, ApJ, 674, 304